2013-07-05

Cryogenic Carbon Capture using a Desublimating Spray Tower

Bradley J. Nielson
Brigham Young University - Provo

Cryogenic Carbon Capture Using a Desublimating Spray Tower

Bradley J. Nielson

A thesis submitted to the faculty of
Brigham Young University
in partial fulfillment of the requirements for the degree of

Master of Science

Larry L. Baxter, Chair
Morris D. Argyle
David J. Frankman

Department of Chemical Engineering

Brigham Young University

July 2013

ABSTRACT

Cryogenic Carbon Capture using a
Desublimating Spray Tower

Bradley J. Nielson
Department of Chemical Engineering, BYU
Master of Science

Global warming is becoming ever increasing concern in our society. As such the likelihood of a carbon tax in the US is becoming increasingly likely. A carbon tax will be expensive enough that coal-based power plants will either have to install carbon capture technology or close. The two front runner technologies for carbon capture are amine scrubbing, and oxyfuel combustion. The downside is that both of these technologies increase power generation cost in a new plant by about 80% and have up to a 30% parasitic load, which reduces the cycle efficiency, that is, the power production per unit fuel consumed, by the same 30%. Retrofitting existing plants by either of these technologies is even more expensive and inefficient since it requires major modifications or replacement of the existing plant in addition to the new capture technology. Sustainable Energy Solutions (SES) has developed a carbon capture technology named cryogenic carbon capture (CCC). CCC is a process by which the flue gas cools to the point that CO_2 desublimates. This process is more efficient, cheaper, and has about half of the parasitic load of other technologies, approaching the theoretical minimum in CO_2 separation within heat exchanger and compressor efficiencies. This thesis conceptually describes, experimentally characterizes, and theoretically models one desublimating heat exchanger as an integral part of the CCC process. A spray tower conceptually developed by SES and theoretically and experimentally explored in previous work at lab scale is developed at bench scale in this work with accompanying major modifications to the theoretical model. It sprays a cold contact liquid to cool warm gas (relative to the contact liquid) that travels up the tower. Nominal operating temperatures are around -120 to -130 °C for 90% and 99% capture, respectively. Once the flue gas cools enough, CO_2 desublimates on the liquid droplet surfaces and forms a slurry with the contact liquid. This spray tower can achieve arbitrarily high CO_2 capture efficiency, depending on the temperature of the exiting gas and other operational variables. The experimental data outlined here varied these operational parameters over broad ranges to achieve capture efficiencies of 55% to greater than 95%, providing a robust data set for model comparison. The operational parameters explored include liquid temperature, liquid flow rate, gas flow rate, and droplet size. These data validated a transport and design model that predicts capture for future scale-up and design of the project. The data and model indicate expected behaviors with most of these variables and a dependence on internal droplet temperature profiles that may be higher than expected. This project significantly advanced the experimental database and the model capabilities that describe the spray tower.

Keywords: Cryogenic Carbon Capture, CCC, carbon capture, desublimating, spray tower

ACKNOWLEDGEMENTS

- My wife, Nicole, for all of her loving support along the way, and for putting up with me being in school for so long
- Dr. Larry Baxter, for all of his help, and for being a great adviser
- Sustainable Energy Solutions, for funding my research
- Dr. David Frankman, for being my mentor and helping me to accomplish things that I never thought I could
- Jeff Bean, for his dedicated work as my assistant, and helping me get everything built and working
- Miguel Lazaro, for all of his experimental work with the shot tower
- David James, for writing the IDT model
- Eric Mansfield, for converting the IDT model to C++

TABLE OF CONTENTS

LIST OF FIGURES

LIST OF TABLES

NOMENCLATURE

Symbol	Property	Units
$\dot{m}$	Mass flow rate	kg/s
$c_{p,i}$	Heat capacity of component i	$\frac{kJ}{kg * K}$
T	Temperature	K
t	Time	s
y	Mole fraction	Unitless
P	Pressure	Pa
P_i^{sat}	Solid vapor pressure of component i	Pa
$\emptyset_i^{sat}$	Fugacity coefficient of component i	Unitless
$\widehat{\emptyset}_i$	Partial fugacity coefficient of component i	Unitless
$\mathcal{F}$	Poynting correction	Unitless
v_i^s	Molar volume of solid component i	$\frac{m^3}{mol}$
r	Radius	m
d	Diameter	m
ρ	Density	$\frac{kg}{m^3}$
k	Thermal conductivity	$\frac{W}{m * K}$
q	Heat Flux	$\frac{W}{m^2}$
v_i	Velocity of component i	$\frac{m}{s}$

NOMENCLATURE CONTINUED

Symbol	Property	Units
g	Gravity	$\frac{\mathrm{m}}{\mathrm{s}^2}$
μ	Dynamic viscosity	$\mathrm{Pa} * \mathrm{s}$
$\boldsymbol{C_d}$	Drag coefficient	Unitless
$\boldsymbol{N_i}$	Molar flux of component i	$\frac{\mathrm{mol}}{\mathrm{m}^2}$
h	Heat transfer coefficient	$\frac{\mathrm{W}}{\mathrm{m}^2 * \mathrm{K}}$
$\boldsymbol{h_m}$	Mass transfer coefficient	$\frac{\mathrm{m}}{\mathrm{s}}$
c	Molar concentration	$\frac{\mathrm{mol}}{\mathrm{L}}$
$\boldsymbol{x_i}$	Mole fraction of component i	Unitless
$\boldsymbol{y_i}$	Mass fraction of component i	Unitless
σ	Surface tension	$\frac{\mathrm{N}}{\mathrm{m}}$
$\boldsymbol{\bar{X}}$	Sample mean	Varies
$\boldsymbol{\mu}$	True mean	Varies
$\boldsymbol{\sigma}$	Standard deviation	Varies
n	Sample size	Unitless
$\boldsymbol{t_{\alpha/2,DF}}$	Two-tailed t-valve at α/2 and DF	Unitless
$\boldsymbol{\alpha}$	Confidence level for t-values	Unitless
DF	Degrees of freedom, $\mathrm{n} - 1$	Unitless

NOMENCLATURE CONTINUED

Symbol	Property	Units
$\boldsymbol{A}$	arbitrary parameter	Varies
$\boldsymbol{B}$	arbitrary parameter	Varies
$\boldsymbol{C}$	arbitrary parameter	Varies
$\boldsymbol{a}$	arbitrary parameter	Varies
$\boldsymbol{b}$	arbitrary parameter	Varies
$\boldsymbol{c}$	arbitrary parameter	Varies
$\boldsymbol{d}$	arbitrary parameter	Varies
$\boldsymbol{e}$	arbitrary parameter	Varies
$\boldsymbol{c}$	speed of light in a vacuum ≈ $2.998\text{x}10^8$	m/s
$\boldsymbol{\mathcal{D}_{im}}$	effective diffusivity of component i in the mixture	$\frac{m^2}{s}$
$\boldsymbol{f}$	arbitrary function of space and time	Varies
$\boldsymbol{f_{1,2,3}}$	values of f at location 1, 2, or 3	Varies
$\boldsymbol{f_2^0}$	Initial value of f_2	Varies
$\boldsymbol{g_r}$	r-component of gravity which (generally 0)	$\frac{m^2}{s}$
$\boldsymbol{n}$	shape parameter	$\frac{N}{m^2} = Pa$

NOMENCLATURE CONTINUED

Symbol	Property	Units
$\boldsymbol{N_A}$	Avogadro constant ≈ 6.02x10^{23}	$\frac{1}{mol}$
$\boldsymbol{q}$	volumetric heat release rate	$\frac{J}{m^3 * s}$
$\boldsymbol{R}$	universal gas constant ≈ 8.314	$\frac{J}{mol * K}$
$\boldsymbol{r}$	spatial dimension	m
$\boldsymbol{r_{1,2,3}}$	spatial location/node	m
$\boldsymbol{r_i}$	molar volumetric production rate of component i	$mol\ of\ \frac{i}{s * m^3}$
$\boldsymbol{\hat{r}_i}$	specific volumetric production rate of component i	$kg\ of\ \frac{i}{s * m^3}$
$\boldsymbol{S_\mu}$	volumetric momentum source term	Varies
$\boldsymbol{v_r}$	radial velocity component	$\frac{m}{s}$
$\boldsymbol{\epsilon}$	emissivity/emittance	Unitless
σ	Stefan-Boltzmann constant $\frac{2\pi^4 k_B^4}{15\ h^3 c^2}$ ≈≈5.67x10-8	$\frac{J}{m^2 * s * K^4}$
$\boldsymbol{h}$	Planck constant ≈ 6.63x10^{-32}	J s
$\boldsymbol{k_B}$	Boltzmann constant $\frac{R}{N_A}$ ≈ 1.38x10^{-23}	$\frac{J}{K}$

NOMENCLATURE (Chemical Species)

Symbol	Property
CO	Carbon monoxide
CO_2	Carbon dioxide
Hg	Mercury
H_2O	Water
NO	Nitric oxide
NO_2	Nitrogen dioxide
NO_x	Nitrogen oxides ($NO + NO_2$)
N_2	Nitrogen
O_2	Oxygen
SO_x	Sulfur oxides ($SO_2 + SO_3$)

1 INTRODUCTION

The earth is able to sustain life in part due to the greenhouse effect. Incident radiation from the sun is mostly in the ultraviolet (UV) and visible regions of the electromagnetic spectrum, most of which passes through the atmosphere without being absorbed. A large fraction of the radiation that passes through the atmosphere is absorbed at the surface of the earth, most of which is remitted as infrared (IR) radiation back towards the atmosphere. The atmosphere absorbs IR radiation much more efficiently than UV or visible radiation because greenhouse gases have significant absorption cross sections in the IR but not in the visible or UV. When the absorbed radiation is re-mitted it radiates in all directions, a large portion of which is directed back to the earth's surface. Additionally, much of the absorbed radiation is transformed into molecular kinetic energy, or heat, warming the atmosphere. This increase in thermal radiation causes the earth's surface and atmosphere to warm enough to support life. Scientists/climatologists estimate that the earth's surface would be an average temperature of -19 °C , 33 degrees below the actual average of 14 °C, if there were no greenhouse effect (Le Treut, Somerville et al. 2007).

All gases with permanent or induced dipole moments effectively absorb IR radiation. This includes water vapor, carbon dioxide, methane, ammonia, and ozone, which are the primary atmospheric constituents involved in the greenhouse effect, but not O_2 or N_2, which are the primary constituents of the atmosphere. Indeed, all heteroatomic molecules have permanent or

induced dipole moments, and are therefore infrared active. There is a lot of environmental concern that increasing concentrations of greenhouse gases in the atmosphere amplify the greenhouse effect, resulting in the surface temperature of the earth increasing. Of all the greenhouse gases, the most concern lies with carbon dioxide, with atmospheric concentrations being 400 ppm, with an approximate increase of 2 ppm per year, largely due to use of fossil fuels (Tans 2012). Water vapor is in much higher atmospheric concentrations and contributes significantly more to the greenhouse effect, but unlike CO_2, manmade contributions to water vapor represent an insignificant fraction of the total atmospheric water concentration and controlling atmospheric water vapor concentrations would be nearly impossible; as well as upsetting the water cycle, which is crucial to our ecosystem. In 2005, global atmospheric carbon dioxide concentrations were 35% higher than they were before the industrial revolution (EPA 2011). A primary reason for this increase is that about 85% of the world's energy comes from some type of combustion process, most of which use fossil fuels. The energy released and harnessed to generate electric power or shaft work comes from combustion reactions that convert hydrocarbons to carbon dioxide and water. Since carbon dioxide is a product of combustion reactions, it cannot be avoided like other pollutants, e.g. SO_x and NO_x.

In 2007 the US Supreme Court ruled in Massachusetts v. EPA (Environmental Protection Agency) that carbon dioxide and other greenhouse gases are covered under the Clean Air Act's broad definition of air pollutants (2007). As a part of that ruling, the Supreme Court mandated that the EPA determine if greenhouse gases endanger public health or welfare. In December of 2009 the EPA released a statement that greenhouse gas pollution threatens Americans' health and welfare by leading to long-lasting changes in our climate that can have a range of negative effects on human health and the environment (EPA 2012). Shortly thereafter, a coalition of states

sued the EPA in an effort to repeal their public endangerment findings and subsequent regulations on greenhouse gases. Three years later, on June 26, 2012, the US Court of Appeals for the D.C. Circuit upheld the EPA's public endangerment findings and their right to regulate greenhouse gases (CADC 2012).

During this same time the EPA decided to regulate mercury and other air toxics (EPA 2012). This includes mercury, nickel, chromium, arsenic, and acid gases. This regulation, the Mercury and Air Toxics Standards (MATS), was proposed on March 16th, 2011 and then finalized it on December 16th 2011. At that time the regulation only applied to existing coal- and oil- fired electric generating units, and the emissions levels were set to the average of the top 12 percent best controlled sources, which are at current technologies limits. A short while later, the EPA proposed the MATS regulation for new power plants on July 20th, 2012 and then finalized it on March 28th, 2013. The regulation for new power plants is even stricter than it is for existing power plants. To meet the standards it will require power plants to be among the most modern and cleanest ever built.

Another proposed regulation was announced on March 27th, 2012. The EPA proposed as part of the Clean Air Act, that power plants built after April 2013 cannot emit more than 1000 lbs. of CO_2 per megawatt hour, which is approximately half of what most coal-fired power plants emit (Jackson 2012). The limit applies to each individual base-load plant, not as an overall cap, but can be averaged over time for a single plant. Codification of this regulation, which does not require formal congressional approval beyond that already granted by the Clean Air Act and its amendments, would mean that no new coal-fired power plants could be built without some form of carbon capture and storage. The limit slightly exceeds the emissions of a modern combined-cycle natural gas plant, but is at or below the emissions of simple-cycle natural gas plants. The

latter, however, are commonly used as peaking plants that follow load fluctuations and do not operate as base-load systems. Such intermittent plants are exempt from the proposed limits (Siemens 2012; Siemens 2012). President Obama announced further CO_2 regulation on June 25, 2013 as a series of executive actions to reduce carbon pollution for new and existing power plants by 50% by 2030 (Obama 2013).

Carbon capture and storage (CCS) is a generic term for processes that separates carbon dioxide from flue gas and stores it permanently, somewhere other than the atmosphere (Wall 2007). Captured carbon dioxide injection provides enhanced or tertiary oil and gas recovery, and produces natural gas from un-mineable coal beds, but once carbon capture becomes commonplace, most of the CO_2 will be sequestered in underground saline aquifers, due to the overwhelming supply. There are competing ideas for storage (deep sea, mineralization, etc.), but most experts agree that saline aquifer injection represents the largest capacity, cheapest process, and lowest technological and environmental risk (Orr 2009; Court, Elliot et al. 2012). While CO_2 storage is an essential component of CCS, the storage itself represents only 1% of the cost, and the combination of transportation, storage, and monitoring represents only 10% of the overall cost of CCS (Ciferno, Litnski et al. 2010). The technological and environmental risk and energy consumption associated with storage are also minimal. The overwhelming portion, approximately 90%, of the cost, and well over 90% of the energy demand and technological risk currently rests with carbon capture.

Power plants have been singled out to solve the increasing atmospheric CO_2 problem for two reasons: first, in the United States they are the single largest source of CO_2 emissions, representing 41% of CO_2 emissions; and second they are stationary, large sources, in contrast to automobiles which combined emit about 30% of the CO_2 in the US, but are mobile which makes

carbon capture more difficult. Most of the remaining 30% of the CO_2 also comes from stationary but generally small-scale sources such as commercial buildings and residences, and effective carbon capture in quantities that could affect climate change (60-80 % of total emissions) requires technology that applies to a large range of sources and scales. Currently CCS is an active research field and a number of technologies have been and are being developed to capture and store carbon dioxide. These technologies can be broken into five categories: oxyfuel combustion, absorption, adsorption, membranes, and cryogenic separation. In the next section, each of these is reviewed in turn. The focus of this work is on the last technology, cryogenic carbon capture, and specifically on the experimental investigation of the performance of a component of this process, a desublimating heat exchanger. The literature review will help place this work in context, after which the specific objectives of the work are outline.

2 LITERATURE REVIEW

2.1 Carbon Capture and Storage

Oxyfuel combustion is the process by which nearly pure oxygen fires power plants instead of air, producing a flue gas stream comprising primarily water and carbon dioxide. The water can be condensed, leaving a nominally pure CO_2 stream. An air separation unit (ASU) built on the front end of such a power plant supplies the oxygen. ASUs cool air to cryogenic temperatures (-200 °C), and then distill oxygen from nitrogen. Due to their similar molecular weights and vapor pressures this is an extremely difficult and energy intensive separation. Firing with pure oxygen also causes increased flame temperatures, which means that the boilers have to be rebuilt and a significant amount of the flue gas has to be recirculated to control the temperatures and heat fluxes. An ASU and oxyfuel combustion decrease plant electrical output by approximately 30% (Wall 2007; Davison and Thambimuthu 2009; Toftegaard, Brix et al. 2010).

Chemical looping is another form of carbon capture. Chemical looping is a process in which oxygen, typically from air, oxidizes a metal oxide particle in an oxidizing reactor, releasing heat, and is then transported to a reducing reactor where it mixes with fuel and converts to a less-oxidized state. This process typically involves two interconnected fluidized beds, which allow the metal oxide particles to circulate between both reactors. Since the metal oxide acts as an oxygen carrier, nitrogen and everything else in air never comes into contact with the fuel and,

more to the point, never mixes with the CO_2 produced from fuel oxidation, thus the flue gas stream will only be water and carbon dioxide, and the separation will be essentially the same as if an ASU unit had been used (Eide, Anheden et al. 2005; Wall 2007; Davison and Thambimuthu 2009). Chemical looping does have its own problems though. The metal oxide particles are expensive and they deactivate with time. More significantly, the cycling temperatures of the metal oxides represent a significant entropy production with associated losses in Gibbs energy. However, if this cycling is done above the maximum steam temperature, little enthalpy is lost compared to a combustion process and the practical Gibbs energy losses are comparable to current power generation systems that lose Gibbs energy by transferring heat from flame temperatures (2000+ K) to comparatively low-temperature water and steam (573-873 K).

The use of an absorption mechanism to capture carbon dioxide includes three categories: chemical, physical, and solid sorbents. The most common and mature of all the carbon capture technologies is chemical absorption. Chemical absorption is the process in which a chemical solvent removes carbon dioxide from flue gas (Rao and Rubin 2002; Wall 2007; Davison and Thambimuthu 2009; Ebner and Ritter 2009; Schreiber, Zapp et al. 2009; Rubin and Zhai 2012). The solvents are typically some type of anime, commonly MEA (monoethanolamine) or MDEA (methyldiethanolamine), which contact the flue gas in an absorption/scrubbing tower. Once the solvent has absorbed CO_2, heat drives the CO_2 from the solution, regenerating the solvent in a stripping tower using steam. As the solvent regenerates, the CO_2 is captured as a pure stream off the top of the tower. The main problem with chemical absorption is the energy cost to regenerate the solvent, which can consume up to 30% of the power plant's capacity. Other problems include degradation and evaporation of the solvent, as well as corrosion of the towers.

Solid sorbent adsorption is very similar to chemical absorption; the primary difference is that a solid sorbent is used instead of a liquid solvent (Eide, Anheden et al. 2005; Davison and Thambimuthu 2009). Metal oxides such as calcium or lithium oxide or natural sorbents such as limestone or dolomite can be used. Solid sorbents are generally used at high temperatures, therefore the energy penalty is lower for regeneration, because the heat required to regenerate is recovered in the capture step. Unfortunately, solid sorbents tend to deactivate quickly, as well introduce the difficulty of solids handling.

Physical absorption is very similar to chemical absorption, but it is performed pre-combustion (after gasification) opposed to post-combustion. The process is ideal for coal-based IGCC plants, where the gas pressure leaving the gasifier is high, thus the partial pressure of CO_2 is high. The increase in the partial pressure allows for the use of a solvent with a lower affinity for CO_2, thus decreasing the energy cost of regeneration (Eide, Anheden et al. 2005; Davison and Thambimuthu 2009). Common physical solvents are methanol, propylene carbonate, and sulpholane.

Adsorption is a physical attraction or affinity between two chemical species, usually between a solid and a gas. This is different from absorption because no chemical bond is actually formed. The right adsorbents will preferentially adsorb CO_2 out of a flue gas stream. Once the adsorbent is saturated it then needs to be regenerated, which is typically done using pressure- (PSA) or temperature-swing adsorption (TSA) processes. Common adsorbents are aluminosilicate zeolites, titanosilcate molecular sieves, and activated carbon (Davison and Thambimuthu 2009; Ebner and Ritter 2009). The adsorption process has even been demonstrated using solid amines (Ebner, Gray et al. 2011). The difficulty with using adsorption for carbon

capture is that PSA/TSA can be energy intensive; in addition the captured CO_2 is generally of low purity.

Membranes can be used for carbon capture based on differences in physical and chemical interactions of flue gas with membrane material, which causes one component to pass through the membrane faster than the other (Eide, Anheden et al. 2005; Ciferno and Marano 2008; Davison and Thambimuthu 2009; Ebner and Ritter 2009). The main advantages of membrane separation are the simplicity of the process, as well as the size; membrane separation processes can be up to ten times smaller than an amine absorption process. The main problem with membranes is that the separation becomes increasingly difficult as the purity of the product stream increases and the technology is fairly young, and much work is still needed. As a result, capture efficiencies are fairly low and costs are fairly high. Membrane technologies are also candidates for oxygen separation in the oxyfuel processes.

2.2 Cryogenic Separation

Cryogenic processes operate on the principle of phase change. Carbon dioxide desublimates as flue gas cools, changing from the gas phase to the solid phase without passing through the liquid phase. Carbon dioxide does not form a liquid phase at any temperature or pressure in the concentrations in which it is typically found in flue gases, up to 16% on a dry, molar basis. Desublimation processes provide essentially pure CO_2, but can suffer high refrigeration costs if poorly engineered. Cryogenic separation is the subject of this research, and this technology review summarizes some of the proposed alternative processes.

Schach et al. conducted a feasibility study of carbon capture by desublimation (Schach, Oyarzun et al. 2011). They modeled the process with Aspen, using finned-plate heat exchangers. The process cooled the incoming flue gas with a condensing heat exchanger. After condensation,

another heat exchanger desublimated remaining water vapor in the flue gas. Finally, a third heat exchanger desublimated the CO_2. In the model, H_2O and CO_2 froze and desublimated directly on the surface of the exchangers; therefore the exchangers need to be regenerated periodically. An economic analysis compared with a standard MEA scrubbing system concluded that while desublimation has superior capture performance with lower energy penalties, the capital costs of a desublimation system are prohibitive. A continuous process avoids regenerative losses by using parallel heat exchanger trains, making it much more attractive.

Clodic et al. have built a desublimating carbon capture system very similar to the one that Schach modeled (Clodic and Younes 2002; Clodic and Younes 2003; Clodic, Younes et al. 2005; Perrotin and Clodic 2005). Their design uses a series of three heat exchangers operating at successively decreasing temperatures. The first condenses water, the second desublimates any remaining water vapor, and the third desublimates carbon dioxide. Clodic uses a flat-plate heat exchanger for the desublimating step, compared to the ideal finned heat exchanger that Schach used in his model. The cold, clean flue gas exits the last exchanger and goes through a regenerative heat exchanger to cool the incoming flue gas. After the CO_2 and H_2O loading in the heat exchangers reaches a maximum (about 10 minutes of operation), the flue gas is diverted into a parallel system and the heat exchangers begin regeneration mode, during which valves isolate them as they warm, melting the CO_2 and pressurizing the system. The water and CO_2 flow out of the heat exchanger as liquids under pressure. The heat exchanger pressure drops back to that of the flue gas, the heat exchangers cool back to cryogenic temperatures, and the process begins again. Challenges with Clodic process include: (1) as CO_2 desublimates it creates an insulating layer between the heat exchanger and the flue gas, which decreases the heat transfer and increases the pressure drop; (2) the system is inherently a semi-batch or batch process; (3), the

amount of CO_2 that is captured is small compared to the mass of the heat exchangers on which it collects, and cycling the large mass of heat exchanger material from the capture temperature of around 140 K to the CO_2 melting temperature of about 220 K generates large amounts of entropy and decreases the process efficiency; and (4) pressurizing the heat exchangers at commercial scale will require a valve that sustains 8-70 bar pressure in a duct that is nominally 30 feet in diameter, which presents a significant practical (rather than fundamental) problem.

Tuinier et al. are currently developing a cryogenic packed bed CO_2 capture process (Tuinier, van Sint Annaland et al. 2010; Tuinier, Van Sint Annaland et al. 2011). Nitrogen initially cools the packed bed. Once flue gas enters the packed bed, water condenses and freezes, then CO_2 desublimates onto the packing material. As the bed reaches maximum H_2O and CO_2 loading, the flue gas is diverted to a parallel system and pure CO_2 flows into the bed above the desublimation temperature but below the freezing temperature of H_2O. The solid CO_2 in the bed sublimates and leaves with the CO_2 stream. Warm nitrogen then evaporates the water, followed by a recycle steam of cold clean flue gas to cool the packing material. This process can be made continuous if three columns are built in parallel.

Song et al. has developed a cryogenic carbon capture technology similar to Clodic, but has managed to make it a truly continuous process (Song, Kitamura et al. 2012; Song, Kitamura et al. 2012; Song, Kitamura et al. 2012; Song, Kitamura et al. 2013). Song uses a similar three heat exchanger design but uses Stirling coolers (SC) instead of plate heat exchangers. A Stirling cooler generates an acoustic pulse that creates a refrigeration effect inside a pulse tube cold finger (Hu, Dai et al. 2010). Stirling coolers have high efficiency, high reliability, and small footprint and volume. The first SC precools and dehydrates the flue gas. The condensed water leaves as a separate stream, while the cool flue gas continues to a second SC. The second SC

desublimates the CO_2 as a solid on the surface of the cold finger, while the clean flue gas exhausts. A mechanical scraping rod is used to keep the surface of that heat exchanger clean, while solid CO_2 falls into a storage chamber where at third SC provides cooling to keep the CO_2 in a solid state. While Song's technology is innovative and has improved upon previous cryogenic technologies, it is still very new with work still needed, especially in the area of scale up.

Researchers at ATK and ACENT Laboratories have taken a very different approach with cryogenic carbon capture. They are currently developing a technology called Inertial Carbon Extraction System (ICES) (ACENT-Labs 2013; ARPA-E 2013). The ICES technology uses a converging-diverging nozzle to accelerate flue gases to supersonic speeds. In reaching supersonic speeds, the gases cool by expansion. The cooling is enough that CO_2 desublimates as solid particles, which are then separated out by a cyclone separator. The technology is mechanically simple, contains no moving parts, generates no chemical waste, and claims to be half as expensive as amine scrubbing technology. To date, however, they have not successfully separated any CO_2 from simulated flue gas.

2.2.1 Cryogenic Carbon Capture

Baxter et al. have and are continuing to develop a process they call Cryogenic Carbon Capture (CCC), originally proposed in a patent disclosure in 2007 (Baxter, Baxter et al. 2009; Baxter, Burt et al. 2009; Baxter 2011). CCC is similar to other cryogenic processes reviewed above in that flue gas cools to the CO_2 desublimation point and then warms in regenerative heat exchangers. It differs in that no heat exchangers cycle temperature or pressure, no parallel streams exist, and all CO_2 compression is done in the condensed phase. These features greatly reduce both the energy and capital/operating costs of the system.

The CCC process exists in two major embodiments, the compressed-flue-gas (CFG) embodiment shown in Figure 1, and the external cooling loop (ECL) embodiment. The major CFG process steps: (1) remove flue gas moisture and cool flue gas to ambient temperatures in a condensing heat exchanger; (2) pressurize flue gas to 5-8 bar for 90-99% CO_2 capture, respectively; (3) cool flue gas to the maximum extent possible using a series of heat recovery heat exchangers (shown as a single unit in the diagram), desublimating about 75% of the CO_2, (4) further cool the flue gas and desublimate additional CO_2 by expansion in a turbine, (5) separate solid CO_2 from the light gases, pressurizing the solids to 8-70 bar, (6) warm both the CO_2 and light gas stream back to ambient temperature in the heat recovery heat exchanger, and (7) pressurize the now liquid CO_2 stream to delivery pressure (typically 125-150 bar). The ECL process is similar except that a refrigerant-bearing external cooling loop supplements heat recovery cooling, eliminating the compression and expansion of flue gas.

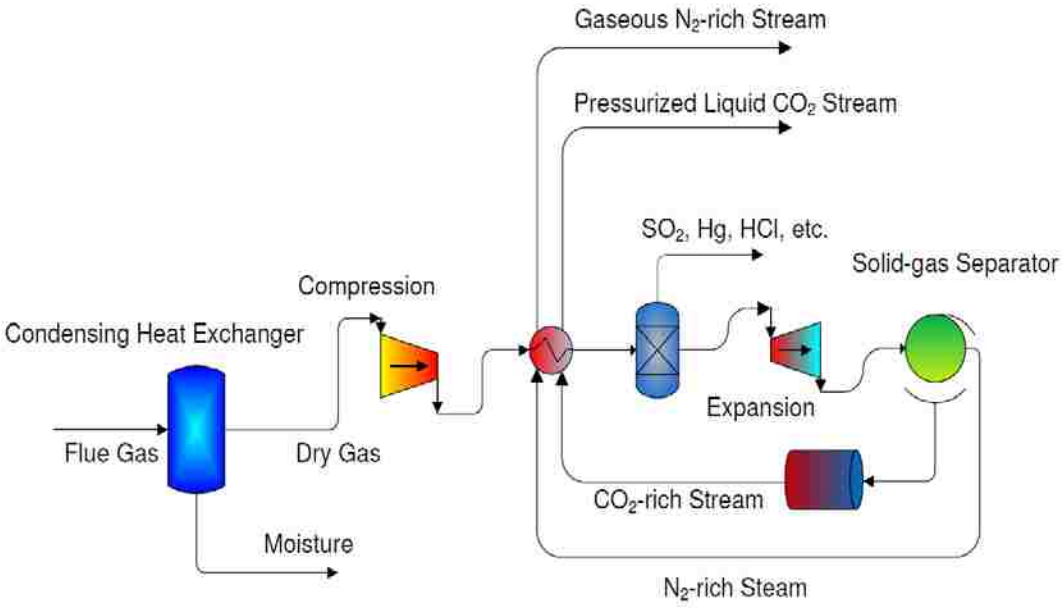

Figure 1: Simple schematic diagram of the cryogenic carbon capture (CCC) process

Both the CFG and ECL processes use desublimating heat exchangers that differ primarily in operating pressure and secondarily in temperature but not in concept or operating principle. In a more detailed analysis, there are several different types of heat exchangers used in the process, all of which appear as a single unit in the process diagram. These include sensible heat exchangers that cool gases to the frost point, melting heat exchangers that melt the solid CO_2, and desublimating heat exchangers, which require the greatest amount of innovation as they must operate continuously and efficiently without fouling or cycling metal temperatures while desublimating solids from the gas. A single desublimating heat exchanger design is the focus of this research.

The CCC process offers significant energy savings compared to competing technologies (Hoeger, Bence et al. 2010). Currently amine scrubbing and oxyfuel combustion represent the de facto standards for carbon capture. The problem is that both technologies consume a significant portion, 25-30% of a plant's capacity. This is because amine scrubbing requires steam regeneration of the solvent, and oxyfuel combustion requires an air separation unit, both of which are extremely energy intensive. Additionally, both processes compress CO_2 gas to about 125 bar in the final steps, which is very energy intensive. Figure 2 shows the approximate parasitic load for CCC, amine scrubbing, and oxyfuel combustion. CCC has a parasitic load of about half that of amine scrubbing and oxyfuel combustion. This is because the CCC process has no large energy drains, such as stream regeneration, an ASU, or temperature cycling. Figure 3 shows the calculated percent increase in the levelized cost of electricity (LCOE) from a power plant operating with any of the listed technologies. The LCOE represents the price of electricity that covers the amortized capital and operating costs of power generation. This graph therefore shows the approximate increase of the cost of electricity generation from building a new power

plant with carbon capture technology, regardless of what type of plant it is. As can been seen CCC has a lot smaller percent increase in LCOE.

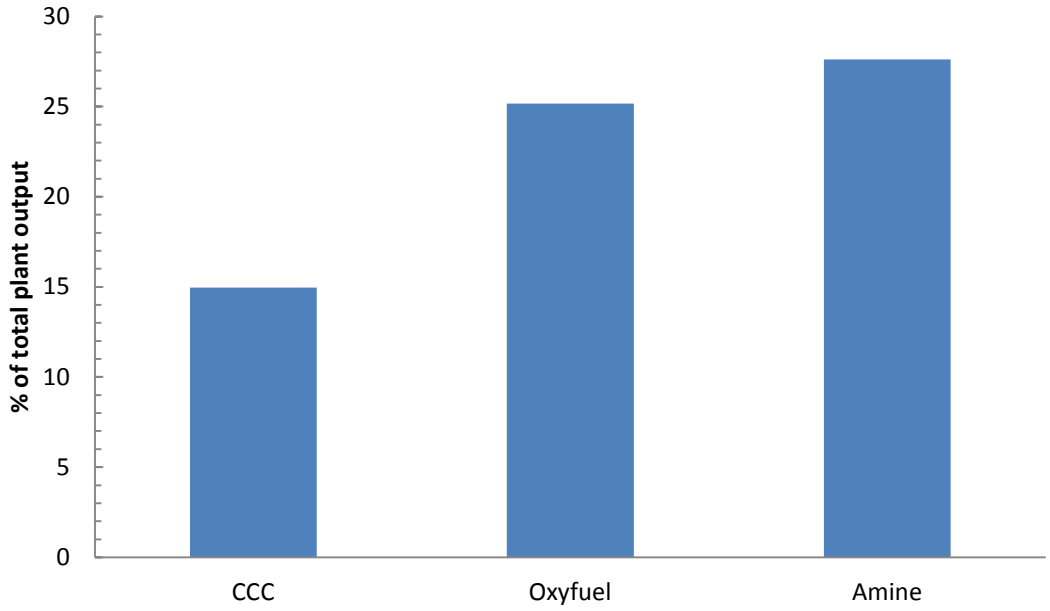

Figure 2: Parasitic load for carbon capture technologies

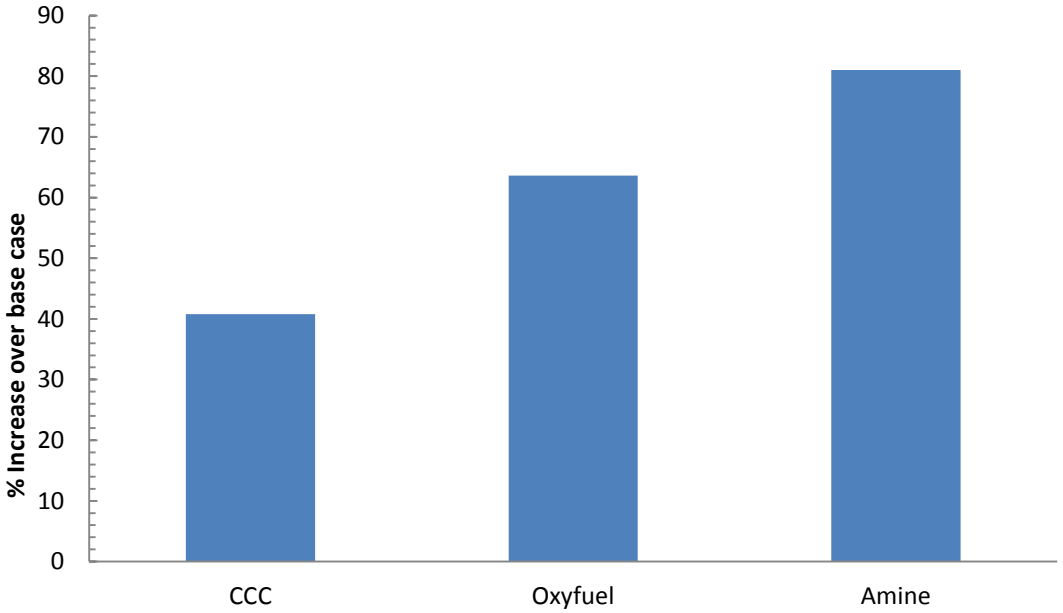

Figure 3: Percent increase of the levelized cost of electricity for carbon capture technologies

Baxter et al. are currently developing three different desublimating heat exchanger designs (Bence, James et al. 2010; Baxter and Bence 2012) as part of the process. These designs are a bubbler, spray tower, and a fluidized bed. The bubbler and the spray tower both use a contacting liquid for direct-contact heat transfer, while the fluidized bed uses cooling rods. All three designs lend themselves to continuous operation with constant temperature profiles, whereas all other designs reviewed are semi-batch processes with non-process elements (heat exchangers or bed materials) cycling in temperature. Another advantage to the CCC process is that it also captures most pollutants. Theoretical and experimental work has shown that this process will capture SOx, particulate, NO_2, HCl, and Hg, the only criteria pollutants it doesn't capture are CO and NO (Larsen, Fox et al. 2010; Larsen, Fox et al. 2010). The focus of this work is on the spray tower, which is reviewed in some detail below.

The spray tower heat exchanger is a vertical tower with counter-current flow, meaning cold liquid droplets fall from the top while comparatively warm flue gas flows up from the bottom. In fact, the tower operates between about 140 K and 170 K, which is a relatively small temperature range and in all cases cold compared to ambient conditions. CO_2 in the gas desublimates on the droplet surface in this countercurrent flow. The solid CO_2 separates from the contacting fluid in a settling chamber and/or a barrier filter after they exit the spray tower, and the contacting fluid is cooled and recirculated back into the tower. The spray tower design generates maximum contact area between the liquid and gas, as the spray nozzle breaks the liquid into fine droplets. The counter-current design maintains a small but nearly constant temperature difference between the gas and liquid streams, which leads to efficient heat transfer. Spray towers also exhibit low pressure drop (Perry, Green et al. 2012). Such a spray tower can

operate over a wide pressure range and are suitable to both the CFG and ECL versions of the CCC process.

In a previous research project in this group, David James modeled the heat and mass transfer that occur in a desublimating spray tower (James 2011) and designed and built one of the initial heat exchangers. His model provides insight into how the capture efficiency changes as design parameters change. The exchanger he designed used solid-sphere shot instead of liquid droplets due to unresolvable safety concerns by the college. Two versions of this "shot tower" and three spray towers have since been built and operated, a portion of which work is the focus of this document. Data from this experimental work will be compared with predictions from the previously mentioned model, and a revised, more detailed model.

3 OBJECTIVE

This project's objective is to build and test the performance of a lab-scale spray tower operating at cryogenic temperatures (140-160 K) with a propriety contact liquid and a flue gas comprising 13-16% CO_2 (dry basis) and the balance N_2. Testing includes experimentation with liquid temperature, liquid flow rate, gas flow rate, and particle size. This data was then used to and validate a predictive model.

Due to limitations of time and resources, this project does not include the following, though many or all of these activities may eventually be done as future work:

- Testing with flue gas from operating boilers
- Measuring capture efficiencies of Hg or other air toxics
- Experimentally integrating the spray tower into the overall CCC process
- Testing the spray tower at elevated pressure

4 EXPERIMENTAL SETUP

This project involved construction and testing of five spray towers, including two towers that used cold lead shot rather than cryogenic liquid and three generations of towers that used cryogenic liquid. The shot tower provided precise control of particle/shot size and avoided using liquid hydrocarbons in the lab. The spray towers represent successive generations of cryogenic handling and design that ultimately provided repeatable results under controlled conditions. Nearly all of the experimental challenges revolved around maintaining cryogenic conditions in a laboratory environment.

4.1 Shot Tower

The first spray tower, Figure 4, comprises a ½" copper pipe, 58" long. Five tees soldered onto the pipe, spaced evenly along the length provide diagnostic access. Three holes through the pipe at the bottom of each tee provide access for a thermocouple and two for gas sampling. The copper tees connect to pipe tees and supported the thermocouple and a gas sample tubes. The gas sample tubes connect through a manifold to a Horiba PG-250 gas analyzer. The manifold allows gas composition sampling from any of the tees along the tower. The bottom tee of the tower serves as a gas inlet, fed by mass flow controllers. Prior to entering the tower, the gas passes through a pre-cooler, which consists of a coiled section of copper tubing in a cold alcohol bath. A 2" thick rigid polyurethane insulation shell surrounds the entire apparatus. A 12" section of 4"

pipe mounted above the tower, reduced to ½" serves as a feeder for the solid shot. The bottom of the tower includes a metal container to collect the lead shot. This tower tested the capture of CO_2 on falling solid spheres at low temperatures. Lead spheres ranging in size from 0.085 to 0.13 inches (2.1 to 3.3 mm) provided size-specific capture efficiency data.

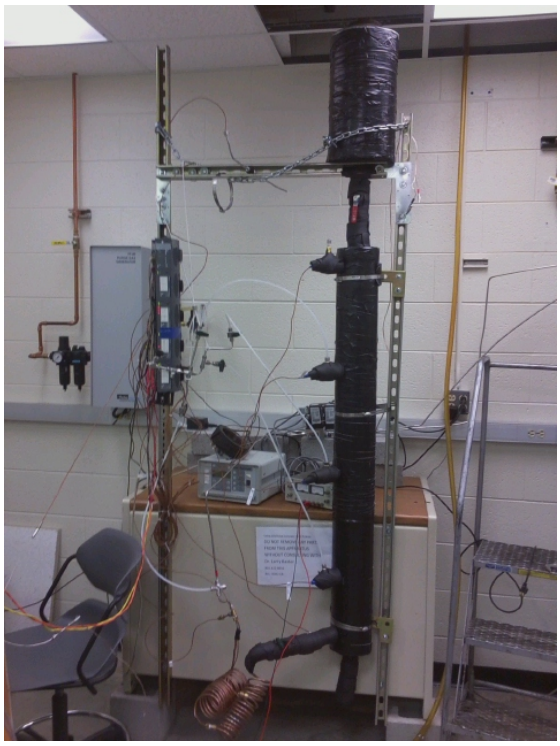

Figure 4: Picture of the shot tower

The first shot tower was too narrow to accommodate the larger shot sizes so a larger tower was constructed. The second tower was built by Miguel Lazaro, an undergraduate research assistant, and was identical to the first shot tower with the exception of diameter, which was twice the size of the diameter in the original tower.

Figure 5 is a process flow diagram of the shot tower. Lead shot cooled with liquid N_2 to ~140 K, was loaded into the reservoir above the tower. A synthetic flue gas, 14% CO_2 and the balance N_2, flowed through the pre-cooler, and cooled to ~175 K before entering the tower. As

the gas flowed up the tower, a valve opened to allow the lead shot to fall down the tower. Lead shot with desublimated CO_2 collected at the bottom of the tower in the shot container, which was in a cold alcohol bath to keep the captured CO_2 from sublimating, while the clean flue gas exited the top of the tower. Gas composition was continuously measured throughout the experiment, with the ability to measure the gas composition from four different places on the tower. LabVIEW monitored, controlled, and recorded the temperature profile and gas composition in the tower.

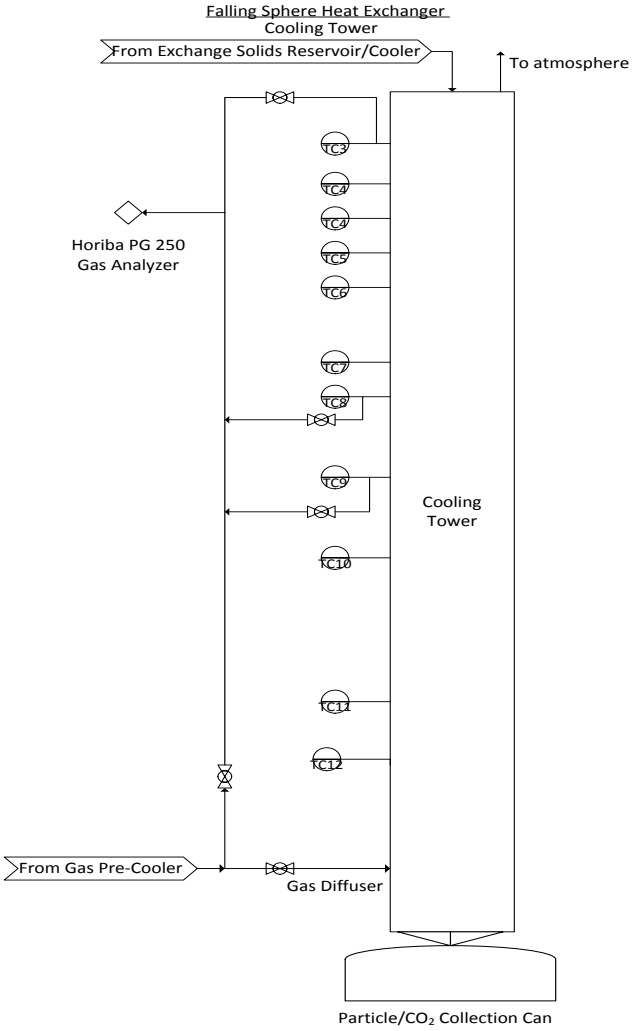

Figure 5: Process flow diagram of the shot tower

4.2 Spray Tower

Three generations of spray tower designs, built and operated at Sustainable Energy Solutions, LLC, ultimately led to a functional system with high capture efficiency, repeatable results, and good control.

4.2.1 Gen 1

The first generation (Gen 1) spray tower, Figure 6, was designed, built and operated by Dr. David Frankman at Sustainable Energy Solutions. The body of the spray tower is constructed of 3" polyvinyl chloride (PVC) pipe, 5' long, surrounded by a larger 8" PVC pipe. The space between the pipes is filled with spray polyurethane insulation; everything else is insulated using rigid polyurethane insulation. The top of the tower is fitted with a showerhead, with a path through it for the clean flue gas. Contacting liquid sprays into the tower and is exposed to simulated flue gas as it flows upward in the tower. Prior to entering the tower, the gas is precooled to ~200 K by flowing through a cooper coil in a cold alcohol bath. The liquid droplets cool the gas to the point that CO_2 desublimates on the surface of the droplets. When the contact liquid/CO_2 slurry droplets reach the bottom of the spray tower, they combine to form a slurry that returns toward the top of the spray tower. Prior to entering the spray tower, the liquid passes through a heat exchanger that cools the contact liquid back to injection temperature using liquid N_2. Contact liquid temperatures are measured at the top and bottom of the tower, as well as before and after the liquid cooler. Gas temperature is also measured at the top and bottom of the tower. All temperature measurements are made using cold-junction-compensated, type T thermocouples. Gas composition is measured using an Enerac 700 integrated emissions system. LabVIEW monitors and records all measurements. There is no method of removing the solid from the contacting liquid, so operation was limited to approximately 15 min.

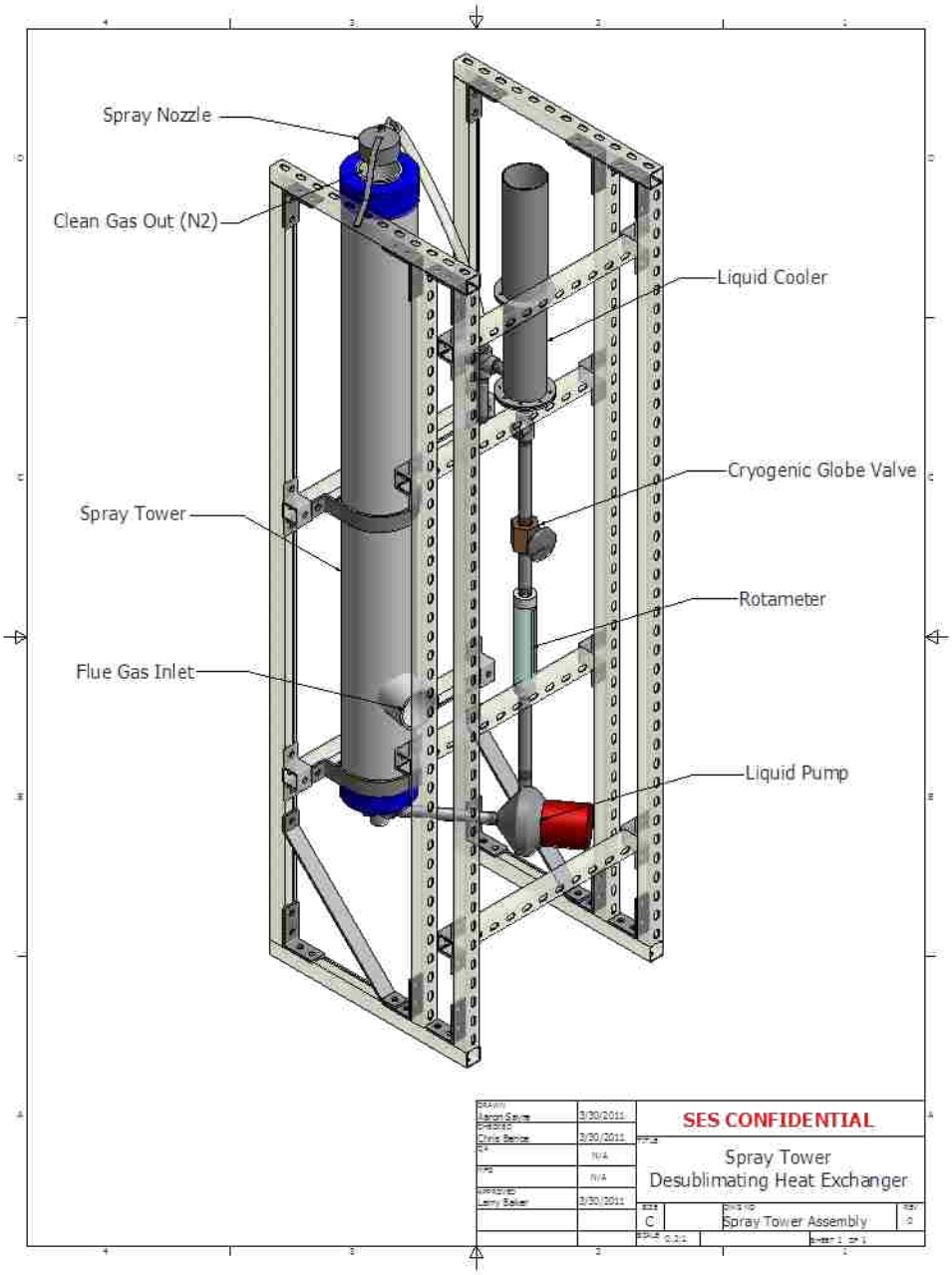

Figure 6: 3D model of the Gen 1 spray tower

The first-generation spray tower served as an excellent proof of concept, but had several failings. First, a rubber coupling used at the bottom of the spray tower was not compatible with the contact liquid. This caused the rubber to become hard and the contact liquid to become discolored. The effect of this on the properties of the contact liquid was unknown, but was

assumed to be undesirable. Second, as the contact liquid was cooled, it became more viscous, which reduced the flow from the pump. This caused the flow from the spray tower to be laminar, and not separate into drops for the first few feet. Third, the viscous contact liquid caused the holes in the showerhead to clog up. Finally, the liquid cooler heat exchanger was not very effective. Since liquid N_2 was used for cooling, it caused the contact liquid to get too cold and freeze on the contacting surface. This, in combination with laminar flow caused the heat transfer to suffer, and the cooling to be cyclical. These shortcomings seriously affected the ability of the spray tower to capture CO_2, so the design was improved with the intention of fixing all of the problems.

4.2.2 Gen 2

The generation 2 (Gen 2) spray tower, Figure 7, was designed, built and operated by Dr. Dave Frankman and the author. Much of the physical and conceptual design of the Gen 1 spray tower was used, so the pump, rotameter, globe valve, and liquid cooler stayed the same. The tower itself was replaced with 3" clear PVC pipe, 5' long, which was covered in 2" thick rigid polyurethane insulation. This was done so that the insulation could be periodically removed to observe the spray in the tower. All the rubber couplings were replaced with PVC couplings. A double wye PVC pipe fitting was added to the top of the tower to allow even and low velocity flow of the gas out of the tower, so as not to entrain any liquid into the gas. A new showerhead was built, that had a removable hole plate. This allowed experimentation with different hole sizes to find the optimal hole size for droplet formation at our operating conditions. Finally baffles were added to the liquid cooling heat exchanger to increase the residence time of the liquid, in an effort to get increased cooling without building a new heat exchanger.

Figure 7: Picture of the Gen 2 spray tower

Due to the similarities between the Gen 1 and Gen 2 spray towers, the experimental procedures were identical. The changes put into the Gen 2 spray tower didn't improve the operation as much as hoped. Specifically, the tower produced relatively low capture efficiencies. The failure of the Gen 2 spray tower was in fact valuable, and helped to narrow the author's focus to the real problem areas of the spray tower.

The clear PVC with removable insulation was nice, because you could see the droplet formation, but the insulation wasn't as thick as before, so the heat/cooling losses increased. When the insulation was removed the tower frosted over quickly, meaning that viewing had to be done very quickly with lots of time between viewing. It ended up being a poor execution of a

good idea. The baffles didn't help the liquid cooler situation significantly. The liquid cooler was still unable to cool the liquid as cold as needed, which was not only the liquid cooler's problem, but also caused by the insufficient insulation. The contact liquid also became too viscous for our centrifugal pump.

The Gen 2 tower was not a complete loss. The double wye worked well as a way to pull gas off the top of the tower uniformly, even though it presented a challenging shape to insulate. The new showerhead also worked well. After experimenting with different hole sizes, good droplet formation was achieved. While the Gen 2 spray tower was unable to reach very good capture efficiencies, it served as a good stepping stone for the next spray tower.

4.2.3 Gen 3

The generation 3 (Gen 3) spray tower, Figure 8, provides repeatable and controllable conditions with high capture. Getting and keeping the contact liquid cold represented one of the major achievements. Acrylic construction provides optical access and viewing in the tower, which proved very helpful during development but will not be a feature of a commercial design. A 4" acrylic tube, 5' long, forms the tower, with a coaxial 5 3/4" acrylic tube around it. The two tubes are connected at both ends and sealed with a 100 Pa vacuum between the tubes, Figure 9. The outer tube is made of two pieces, allowing it to adjust in length as the pieces slide past each other during thermal contraction. This vacuum jacket of insulation allows for continuous observation without frost formation.

Figure 8: Picture of the Gen 3 spray tower

The incorporation of an insulation jacket, while useful, also introduces some challenges. The primary challenge is the method of introducing the gas into the spray tower. All previous designs used side ports above the liquid level for gas entry. Since the vacuum jacket couldn't be penetrated, the gas has to be introduced into the Gen 3 tower from the bottom without allowing droplets to enter and without desublimating on the walls as it flows through the liquid pool. In the Gen. 3 design, the gas enters the tower through a concentric, vacuum-insulated tube similar to the spray tower that passes through the accumulated slurry pool at the bottom of the tube. The double wye and showerhead are used from the Gen 2 spray tower, with essentially every other feature changed as described above.

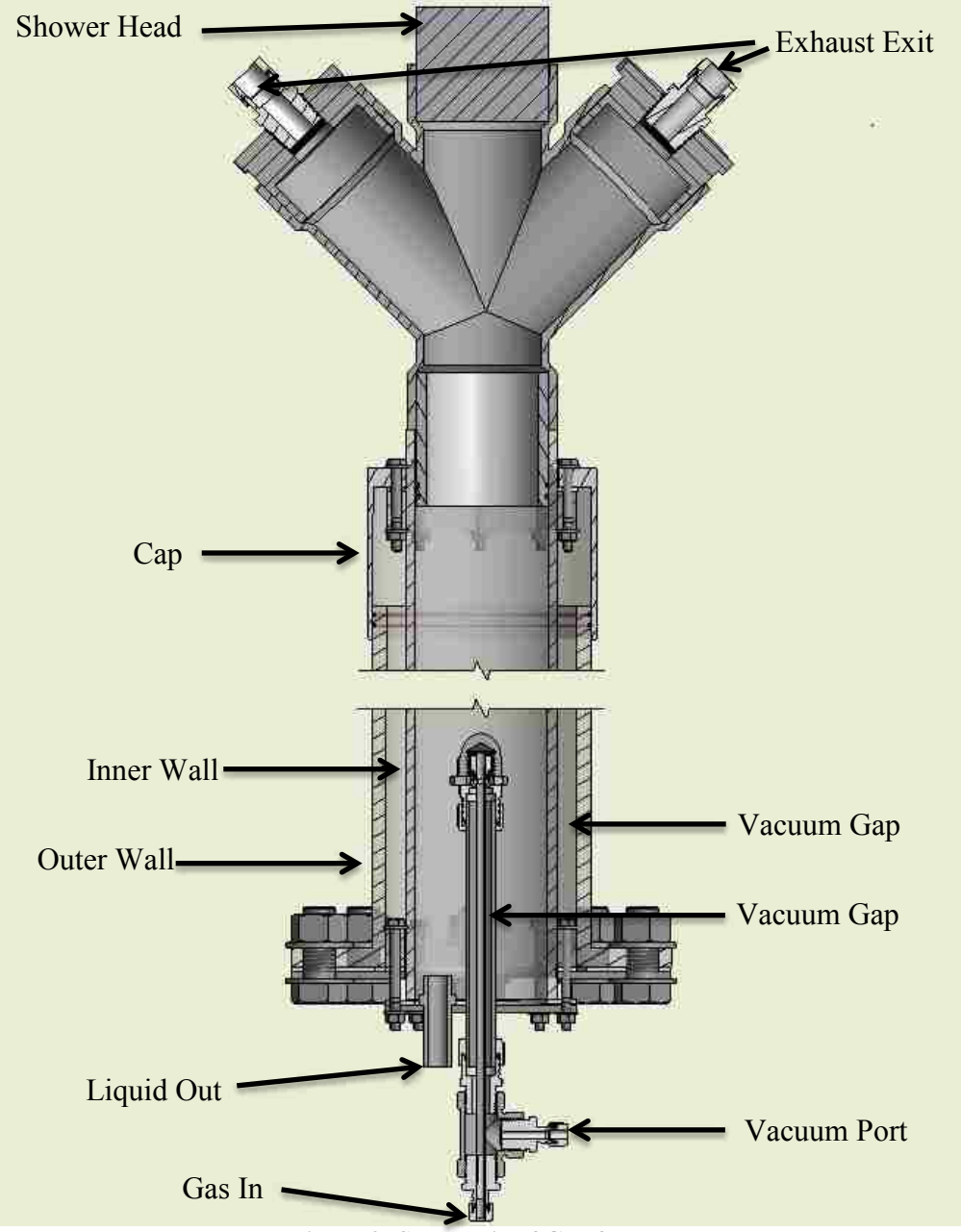

Figure 9: Schematic of Gen 3 spray tower

An experimental platform, code named Sylvia 87, Figure 10, provides infrastructure support for the spray tower, as well as other experiments at Sustainable Energy Solutions. (Major facilities at SES have names that correspond to astronomical bodies with average surface

temperatures comparable to their operating temperatures. Sylvia 87 is one of the largest asteroids and is classified as a dwarf planet. It has two moons – Remus and Romulus – and an average surface temperature of 151 K.) In essence, Sylvia provides both liquid and gas cooling to run this and other experiments. Sylvia needs only to connect the liquid and gas in and out lines to a heat exchanger. Figure 11 shows the major components of Sylvia. Sylvia uses a gear pump to provide high liquid flowrates of potentially highly viscous fluids without leakage at cryogenic temperatures. Sylvia includes two brazed-plate heat exchangers. The first cools the contact liquid and exchanges heat with refrigerant from a Polycold Fast Cycle Water Vapor Cryopump. The second recuperates heat, or in this case cooling, to precool the flue gas; the outgoing clean gas cools the incoming flue gas. Sylvia includes a liquid reservoir, so that the contact liquid doesn't have to be stored inside the desublimating heat exchanger. Sylvia also includes mass flow controllers, thermocouples, pressure transduces, a gas analyzer, and a National Instruments DAQ system to acquire and record all data from experiments. A new form of insulation is also used; Sylvia has three cold boxes, which are filled with perlite insulation. Figure 12 shows a process flow diagram for Sylvia. LabVIEW programs control, monitor, and record all the data from all the equipment and instrumentation on Sylvia. Further details about the LabVIEW program can be found in the appendix.

Figure 10: Picture of Sylvia 87

4.3 Experimental Variables

The Gen 3 spray tower provides a flexible and robust experimental basis for determining which factors affect CO_2 capture. The underlying motivation for this in addition to establishing a fundamental understanding of the tower operation is to be able to create an accurate model to use for design of future spray towers, such as scaled-up versions. Gas flow rate, liquid flow rate, and liquid temperature vary over the ranges indicated below, Table 1, in experiments done with the spray tower. The shot tower provided data as a function of shot size, Table 2. CO_2 capture as a function of the following experimental variables provided a data set for model validation.

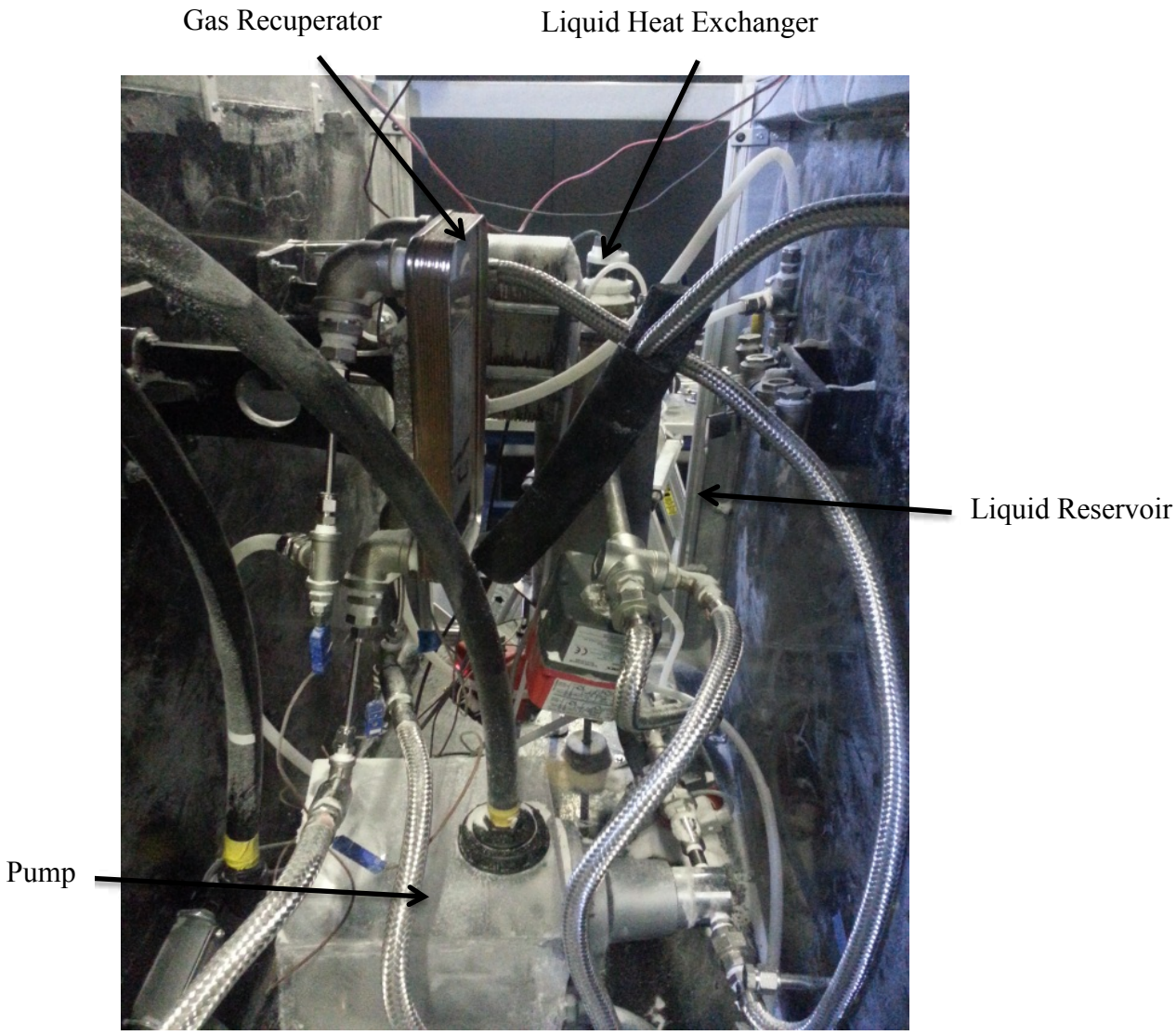

Figure 11: Internal components of Sylvia

Table 1 Experimental design space for independent variables in the spray tower

Variable	Range
Inlet Liquid Temperature	150 - 161 K
Inlet Gas Temperature	235- 285 K
Liquid Flow Rate	5 – 15 lpm
Gas Flow Rate	0.2 – 2.5 scfm
Gas Velocities	0.015 - 0.19 m/s

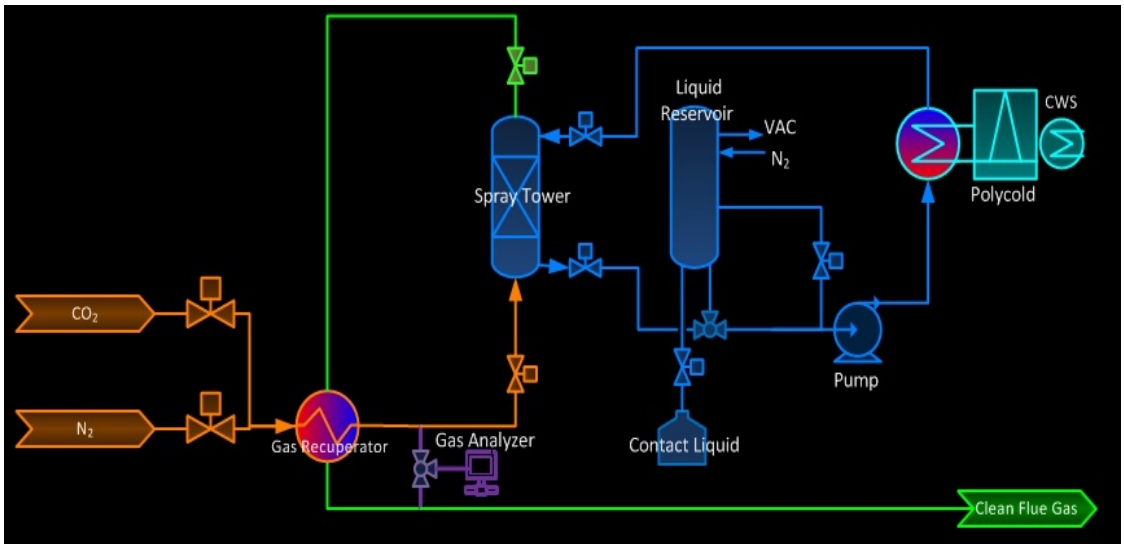

Figure 12: Process flow diagram for Sylvia

Table 2 Experimental design space for independent variables in the shot tower

Variable	Range
Inlet Shot Temperature	120 – 180 K
Inlet Gas Temperature	175 – 185 K
Shot Flow Rate	0.08 – 0.19 kg/s
Shot Size	2 – 3.3 mm
Tower/sample Height	0.7 – 3.3 m

5 RESULTS AND DISCUSSION

5.1 Model

Having a model that accurately predicts carbon capture in a spray tower is more important than the spray tower itself. A model can optimize operation or scale-up a design, without having to run experiments. The objective of this research was not to only build a lab-scale desublimating spray tower it was also to use the experimental data and a theoretical model to develop a predictive understanding and quantitative design tool for the spray tower.

5.1.1 Isothermal Drop Transport Model

A previous graduate student in our research group, David James, wrote a model to predict carbon capture in a desublimating spray tower, the Isothermal Drop Transport (IDT) model. The model simultaneously solves the mass, momentum, and energy transport equations for a system in which gaseous CO_2 is desublimating onto liquid droplets. The model assumes a spherical droplet that falls through a plug-flow tower with 128 nodes before reaching the bottom. One-dimensional, steady-state mass, energy, continuity, and momentum equations predict the gas and droplet compositions, temperatures, and velocities for each node, which results in predictions for temperature, velocity, pressure, gas composition, and heat and mass transfer rates as a function of residence time and position. The IDT model predictions were compared with preliminary data from two versions of the shot tower at the time it was written (James 2011). The IDT model is

coded in Visual Basic for Applications as part of an Excel spreadsheet. The model agreed reasonably well with the high capture efficiency data available at the time, though its convergence was both slow and unstable.

The IDT model predicts carbon capture for the broader range of operating conditions represented by the data collected in this work with reasonable agreement at high capture efficiencies progressing to poor agreement at lower capture efficiencies. The reasons for the poor agreement were initially not clear, though it later became clear that a major contributing factor is the isothermal droplet assumption. The preliminary data available for model validation for the IDT model used lead shot as "droplets." Lead has a much higher thermal conductivity than contacting fluid, which significantly decreases internal temperature gradients. The IDT model predicts greater capture than actually observed, except when the contact liquid was below 150 K, which generates reasonable predictions. Figure 13 shows carbon capture vs. liquid temperature data for experiments done with a gas flow rate at one standard cubic foot (scfm). The solid line above the data points shows IDT model predictions for the same conditions. Figure 13 is a representative example of the discrepancy between the IDT model and experimental data. Figure 14 is a parity plot of predicted vs. measured capture for all experimental data. The 45° line represents perfect agreement between measured and predicted results. As can be seen, very few data points are on or even close to the 45° line.

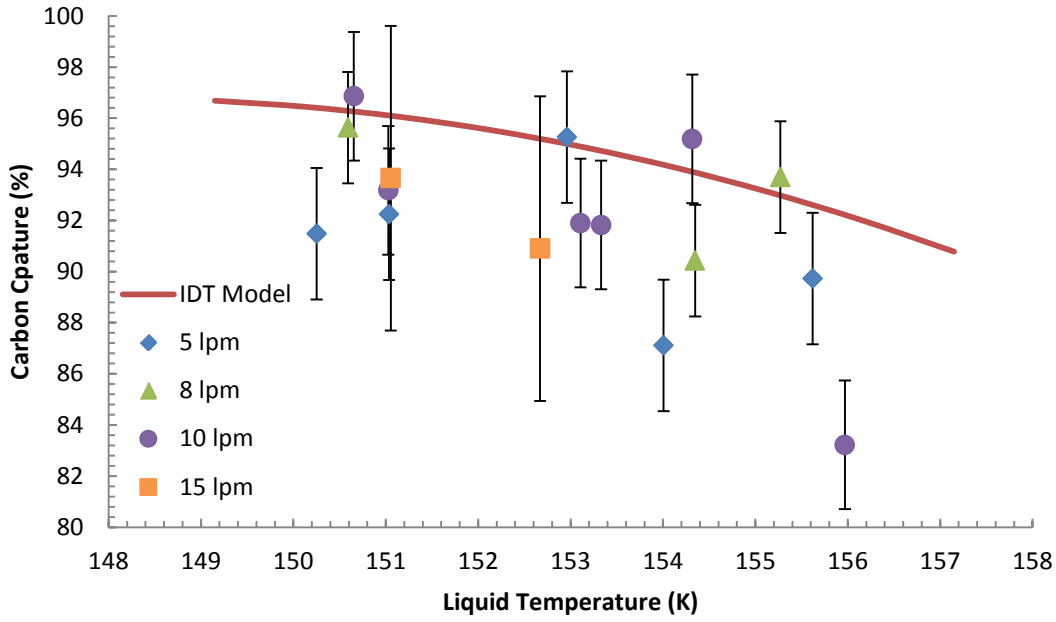

Figure 13: Percent carbon capture vs. liquid temperature for experiments done at 1 scfm, as well as predictions from the IDT model

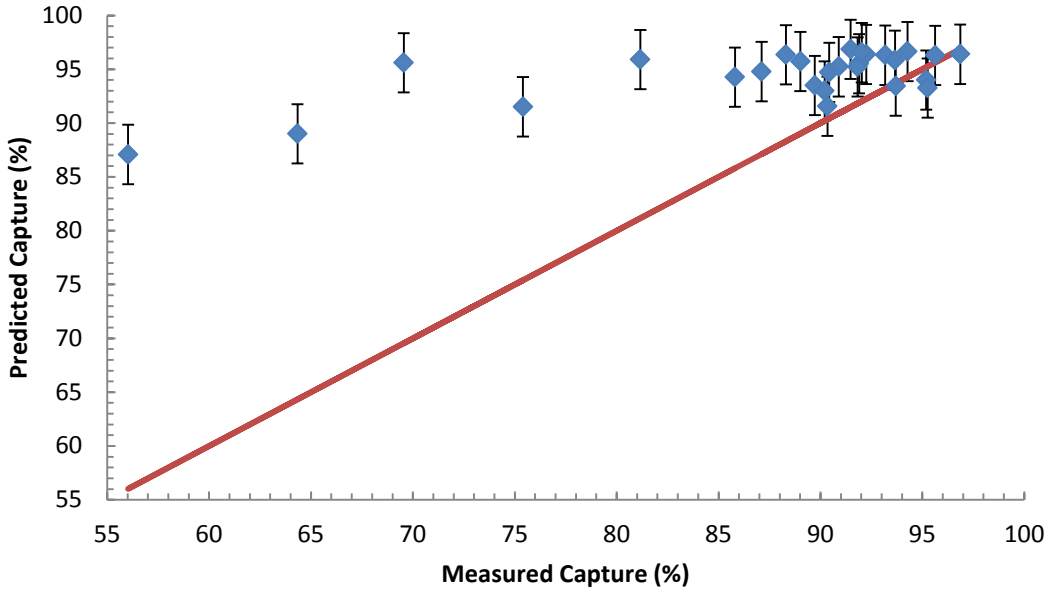

Figure 14: Parity plot of predicted vs. measured capture using the IDT model

The error bars shown, and all future error bars, display a 95% confidence interval. Confidence intervals are calculated using the following equation

$$\bar{X} - t_{\propto/2,DF}\frac{\sigma}{\sqrt{n}} \leq \mu \leq \bar{X} + t_{\propto/2,DF}\frac{\sigma}{\sqrt{n}} \quad (1)$$

where $\bar{X}$ is the sample mean, μ is the true (population) mean, σ is the sample standard deviation, n is number of samples in the data set, $t_{\propto/2,DF}$ is the corresponding t-value in the two-tailed table, and DF is the degrees of freedom which is equal to $n - 1$.

The difference between the measured and predicted capture for each data point is calculated. These differences are then organized into data sets based on experimental conditions. The sample standard deviation, σ, is then calculated by calculating the standard deviation of the differences for each data set. The sample size, n, is determined by the number of data points inside a data set.

5.1.2 Equilibrium Model

The shortcomings of the IDT model prompted a search for a better model. A better model was obtained by using an equilibrium calculation compared to the prior transport calculation. Despite the simplicity of the model, the predictions were much better. The equilibrium model was obtained simply by calculating how much CO_2 would be in the solid phase if the system were at local equilibrium. Surprisingly, it appears that many of the data points taken from the spray tower are at or near an equilibrium state.

The equilibrium capture efficiency and other properties involve solving a system of three differential equations, an enthalpy balance, a mass balance, and a solid-vapor equilibrium equation. The enthalpy balance is

$$\dot{m}_{N_2} C_{p,N_2} \frac{\partial T}{\partial t} + \dot{m}_{liq} C_{p,liq} \frac{\partial T}{\partial t} + \dot{m}_{CO_2(g)} C_{p,CO_2(g)} \frac{\partial T}{\partial t} + \dot{m}_{CO_2(s)} C_{p,CO_2(s)} \frac{\partial T}{\partial t} - \dot{m}_{CO_2(s)} H_{sub} = 0 \quad (2)$$

where $\dot{m}$ is the mass flow rate, $C_{p,i}$ is the heat capacity of component i, and $\frac{\partial T}{\partial t}$ is the partial derivative of temperature in terms of time. The mass balance was calculated using the following relationship

$$\dot{m}_{CO2in} = \dot{m}_{CO2(g)} + \dot{m}_{CO2(s)} \quad (3)$$

The solid-vapor equilibrium depended only on the thermodynamics as indicated by the following

$$y_{CO2} = \frac{P_{CO2}^{sat}}{P} \frac{\emptyset_{CO2}^{sat}}{\widehat{\emptyset}_{CO2}} \mathcal{F} \quad (4)$$

where y_{CO2} is the mole fraction of CO_2 in the gas phase, P_{CO2}^{sat} is the solid vapor pressure of CO_2, P is the total pressure of the system, $\emptyset_{CO2}^{sat}$ is the fugacity coefficient of CO_2 evaluated at P_{CO2}^{sat}, $\widehat{\emptyset}_{CO2}$ is the partial fugacity coefficient of CO_2, and $\mathcal{F}$ is the Poynting correction. The Poynting correction can be calculated by the following

$$\mathcal{F} = exp\left[\frac{v_{CO2}^{s} * (P - P_{CO2}^{sat})}{RT}\right] \quad (5)$$

where v_{CO2}^{s} is the molar volume of solid CO_2, and R is the ideal gas constant.

Figure 15 displays the same experimental data shown in the previous section, data taken with a gas flow rate of 1 scfm, but this time the model predictions are using the equilibrium model. The data exhibit some scatter, but they include data taken at different liquid flow rates (5, 8, and 10 lpm), as well as small differences in gas temperature. The model prediction shown assumes a liquid flowrate of 5 liters per minute (lpm), with a gas flow at 273 K and 1 scfm. A prediction for 15 lpm is indistinguishable from the 5 lpm prediction shown. Despite the scatter, the equilibrium model prediction appears to go through the median of the data. While the model matches this data set fairly well, that isn't the case for all of the data.

Figure 16 shows carbon capture vs. liquid temperature data for all spray tower experiments, along with the equilibrium model predictions for the same temperature range. When the model is compared across a larger temperature range, it is clear that the model is not rigorous enough, which can be seen be looking at the right side of Figure 16. One hypothesis for the discrepancy is that when the temperature of the contact liquid is near the temperature required to desublimate CO_2, the CO_2 will start to desublimate onto the surface of the drop, but then due to the heat of desublimation, the surface temperature increases, decreasing the amount of CO_2 that desublimates. This temperature rise causes an overall decrease in carbon capture. This effect, in combination with high gas flow rates and low liquid flow rates in that region, cause the model to deviate from the data.

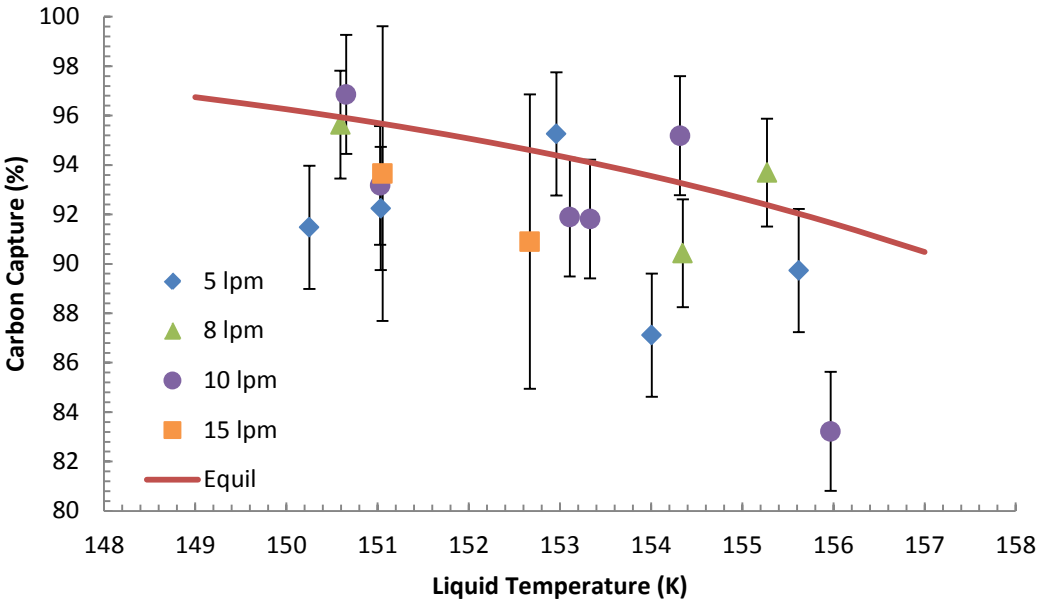

Figure 15: Percent carbon capture vs. liquid temperature for experiments done at 1 scfm gas flow rate, as well as predictions from the equilibrium model

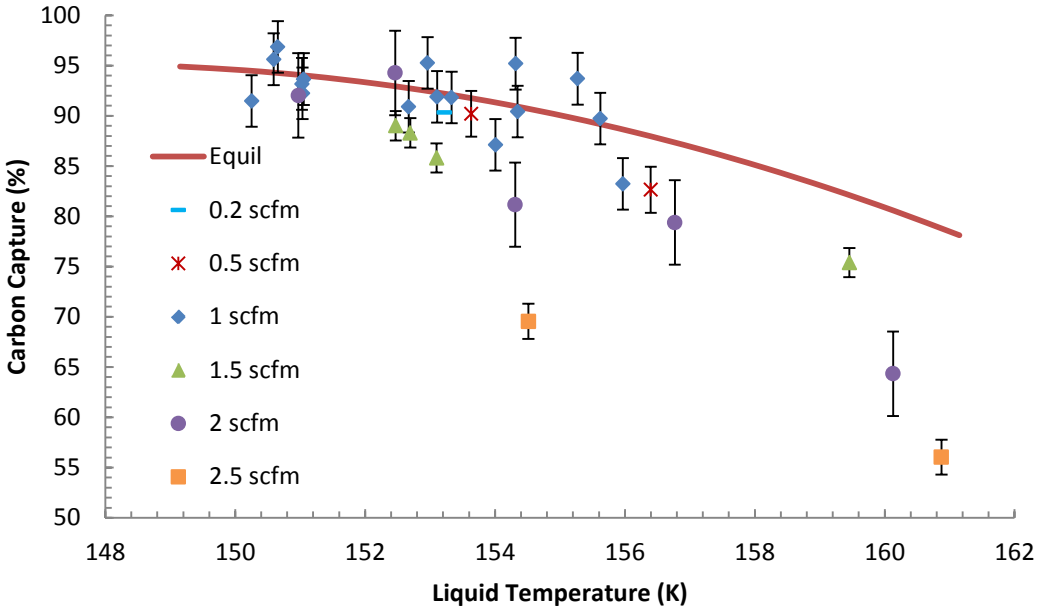

Figure 16: Percent carbon capture vs. liquid temperature for all experiments, as well as predictions from the equilibrium model

Figure 17 is a parity plot of predicted vs. experimental capture for all experimental data. Many more of the data points are on or near the 45° line, but there is still room for improvement. To model the effects that occur when the liquid temperature is near the desublimation point, when the gas flow rate is high, and when the liquid flow rate is low, a transport model was revisited.

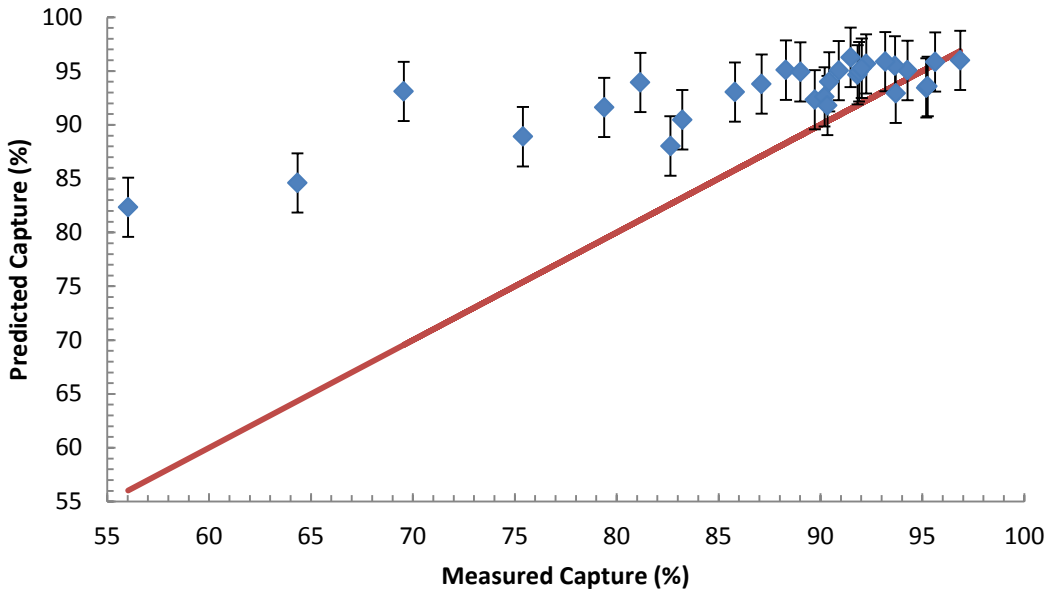

Figure 17: Parity plot of predicted vs. measured capture using the equilibrium model

5.1.3 Droplet Temperature Gradient and Transport Model

Both the IDT and the equilibrium model failed to model the data sufficiently. This was because both models made assumptions that turned out to not hold true in all cases. To model the data better, Dr. Baxter wrote a new transport model using fewer assumptions. The new model, the Droplet Temperature Gradient and Transport (DTGT) model, solves 1-dimensional mass, momentum, and energy transport equations in the tower for the gas phase, but also calculates dynamic internal temperature gradients in the particles. As will be shown, the particle surface

heats up significantly as CO_2 desublimates, which ended up being the major downfall of the two previous models. The particle size, composition, temperature profile, and mass are all treated in a dynamic fashion. As CO_2 desublimates on the particle both size and mass increase. The thermal conductivity of the particle varies with temperature and composition. In addition, a more rigorous numerical method was used, to make the model more robust and converge much faster. Despite solving the internal droplet gradients at each computational step in addition to the gas gradients as a function of position, this model runs far faster and is far more stable than the IDT model. A single tower simulation with a single droplet starting position requires about 10 seconds with this model on a modern computer, as compared with many hours with the IDT model. The increases in computational efficiency and stability come from, in approximate order of importance, the code structure, advanced numerical methods, vector processing (which is done with the computer graphics processing unit (GPU), rather than entirely with the central processing unit (CPU)), rigorous optimizations, parallel processing, and advanced features of the C++ programming language (valarrays, delta functions, and function templates).

Radial profiles were included in the gas stream. As the flue gas travels up the spray tower, the gas in the center of the tower moves the fastest with the velocity decreasing closer to the walls, reaching zero velocity at the wall. The velocity profile causes lower capture in the center of the tower due to the faster gas velocity, and higher capture around the edges of the tower. When the capture is integrated across the radius of the tower an overall capture decrease is produced compared to assuming uniform radial properties at each axial node. The experimental results agree with these details of the predictions.

As mentioned before the transport model simultaneously solves the transport equations. The energy transport equation for the droplet is

$$\rho\left(C_p\frac{\partial T}{\partial t}+v_r\frac{\partial T}{\partial r}\right)=-\frac{1}{r^n}\left(k(r)r^n\frac{\partial T}{\partial t}\right) \tag{6}$$

where ρ is density, C_p is heat capacity, T is temperature, t is time, v_r is the radial component of velocity in the droplet, r is radius, n is a shape parameter that is two for a spherical droplet as generally assumed here, and $k(r)$ is the spatially dependent thermal conductivity. The energy PDE is solved using a symmetry condition, specified flux, and an initial condition, as follows.

$$T(t=0)=T_0 \tag{7}$$

$$\left.\frac{\partial T}{\partial r}\right|_{r=0}=0 \tag{8}$$

$$-k\left.\frac{\partial T}{\partial r}\right|_{r=R}=q_{surf}+h\theta(T_s-T_b) \tag{9}$$

where T_0 is the is the initial particle temperature, q_{surf} is the heat flux at the surface of the particle associated with CO_2 desublimation, T_s is the surface temperature of the particle, T_b, is the bulk gas temperature, h is the heat transfer coefficient, and θ is the blowing factor, which is near one for nearly all conditions in this experiment. All of these properties depend on position in the tower or, equivalently, residence time in addition to the indicated dependencies on radial position in the droplet.

The momentum transfer was solved used is the following

$$\frac{dv_p}{dt} = -\beta(v_p - v_g)|v_p - v_g| + \left(1 - \frac{\rho_g}{\rho_p}\right)g \tag{10}$$

where v_p is the velocity of the particle, v_g is the velocity of the gas, ρ_g is the density of the gas, ρ_p is the density of the particle, g is the acceleration due to gravity, and β is

$$\beta = \frac{3C_d\rho_g}{4d_p\rho_p} \approx \frac{18\mu_g}{d_p^2\rho_p} \tag{11}$$

where C_d is the drag coefficient, which is a function of the Reynolds number, d_p is the particle diameter, and μ_g is the viscosity of the gas. The last expression above is for droplets in the Stoke's regime. These droplets commonly were not in the Stoke's regime, in which case the more rigorous but empirical correlation for C_d (Polezhaev and Chircov 2011) as a function of Reynolds and Mach number was used based on our own measured data. The correlation is

$$C_d^0 = \frac{a}{Re} + b + c\ln(Re) + d\ln(Re)^2 + e\ln(Re)^3 \tag{12}$$

$$C_d = C_d^0 \frac{1 - 0.445Ma + 4.84Ma^2 - 9.73Ma^3 + 6.93Ma^4}{\sqrt{1 + 1.2MaC_d^0}} \tag{13}$$

where a, b, c, d, e are fitted coefficients that can be found in Table 3, and Re is the Reynolds number, Ma is Mach number, and C_d^0 is the drag coefficient uncorrected for Mach number.

Table 3 Fitted coefficients for empirical C_d correlation

Coefficient	Value
a	136666.5755
b	-12.22779178
c	1.567641782
d	-0.049494065
e	-5.72304E-06

The mass transfer rate depends on gas properties according to the equation

$$N_{CO_2} = h_m \theta c (x_{CO2s} - x_{CO2b}) + x_{CO2s} \sum N_i \tag{14}$$

where N_i is the molar flux of component$i$, h_m is the mass transfer coefficient for species i, c is the molar concentration of the gas, x_{CO2s} is the mole fraction of CO_2 in the gas at the droplet surface, and x_{CO2b} is the mole fraction CO_2 in the bulk gas phase. All of these variables depend on axial and radial position in the tower. A similar equation for the concentration of the vapor associated with the liquid droplets was also solved.

In both cases, the height dependence of the gas-phase species is determined by integrating the expression for the flux such as are indicated above over the grid in the z/height direction at each radial node and calculating source/sink terms for the species. These are included in gas-phase continuity equations to determine the gas-phase species composition. The

predictions indicate that in many conditions, all of those in which the droplet surface temperature rises above its frost point, the CO_2 content of the gas actually increases near the bottom of the tower as some of the CO_2 that desublimated in the top of the tower resublimates in the bottom.

The drop size for the model was determined by using a correlation taken from Perry's Chemical Engineers' Handbook for viscous liquids (Perry, Green et al. 2012). The correlation is as follows:

$$d = 1.89 d_j \left[1 + \frac{3\mu}{\left(\sigma \rho d_j\right)^2} \right] \tag{15}$$

where d is the drop diameter, d_j is the hole diameter, μ is the dynamic viscosity, σ is the surface tension.

The droplets were quite viscous at these temperatures, but they were still liquid. The model could alternatively assume both that the CO_2 solid formed a skin on the droplet and that it was quickly pulled into the droplet via surface tension forces. The predictions shown here make the latter assumption, which seems the most likely though there are no data to support either assumption. The high viscosity of the liquid minimized internal recirculation of the droplet liquid.

The predications with this model were a marked improvement over the previous models. Figure 18 is a parity plot showing predicted vs. measured CO_2 capture using the DTGT model. Most of the points are very close to the 45° line, with only a few exceptions. The average percent error between the measured value and the predicted value is 2.31%, whereas the average 95% confidence interval is ±2.75%. Figure 19 displays a comparison of parity plots for all the

different models including the most significant individual contributions as determined by the most detailed transport model. These include heat, mass, frost, and velocity profile effects. Nevertheless, there remain some data points whose confidence intervals do not include the predicted results. It is not clear at this point if these represent spurious data of a lack of sufficient model rigor.

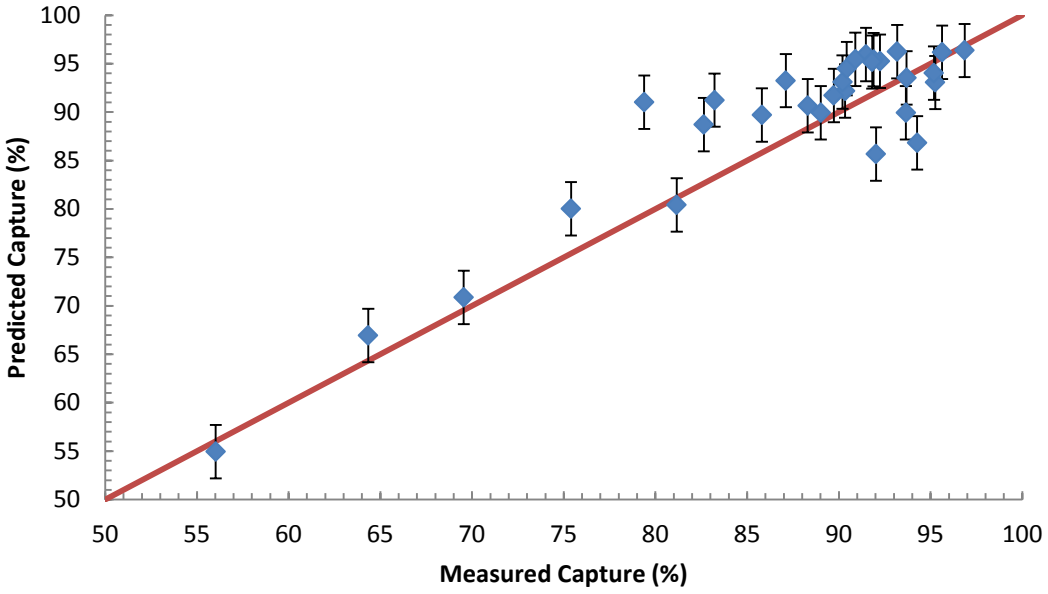

Figure 18: Parity plot of predicted vs. measured capture using the DTGT model

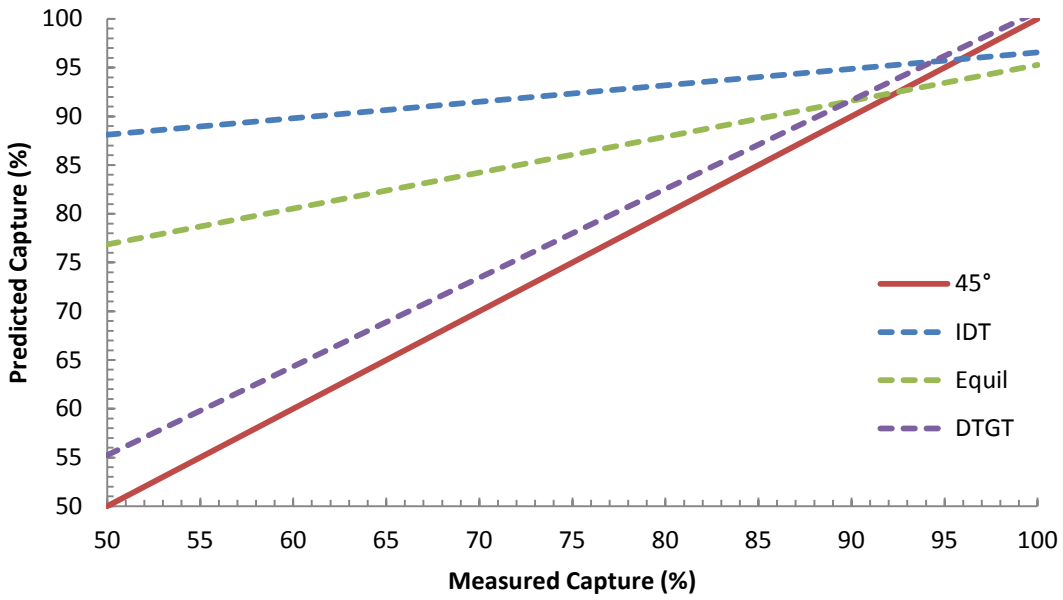

Figure 19: Parity plot comparing all the different models

5.2 Trends

The capture of CO_2 from flue gas depends primarily on initial liquid temperature followed by particle size, gas flow rate, liquid flow rate, and initial gas temperature. In the course of experimentation all of these variables were investigated, and their associated effects are discussed below. Other factors affect the capture of CO_2, but were not included in this investigation. In addition the temperature profile through the tower and the particle are also presented.

5.2.1 Liquid Temperature

The flue gas temperature primarily determines the degree of CO_2 desublimation, with CO_2 transport to the droplets playing a secondary role and heat transfer a primary role in determining flue gas temperature. The spray tower cools the gas by convective heat transfer from

the contact liquid, leading to increased CO_2 capture with decreased droplet temperature, all else being equal.

Figure 20 shows the percent solid CO_2 vs. temperature for different CO_2 compositions, using a solid-vapor equilibrium calculation. Percent solid CO_2 is the percent of CO_2 in the solid phase, whereas the percent CO_2 is the percent CO_2 in the gas. The balance of the gas is nitrogen. The calculation is done using the Soave-Redlich-Kwong equation of state along with the version of the solid-vapor equilibrium equation that includes both fugacity and activity coefficients. Figure 20 shows that as the concentration of CO_2 in the mixture decreases the temperature required to desublimate all of the CO_2. To achieve 90% capture for a 15% CO_2 mixture (average for coal fired power plant flue gas) a temperature of ~155 K must be reached, but if 99% capture is desired the temperature must be decreased to ~140 K. While equilibrium calculations are a decent approximation, transport effects need to be considered if operating conditions produce a non-equilibrium state.

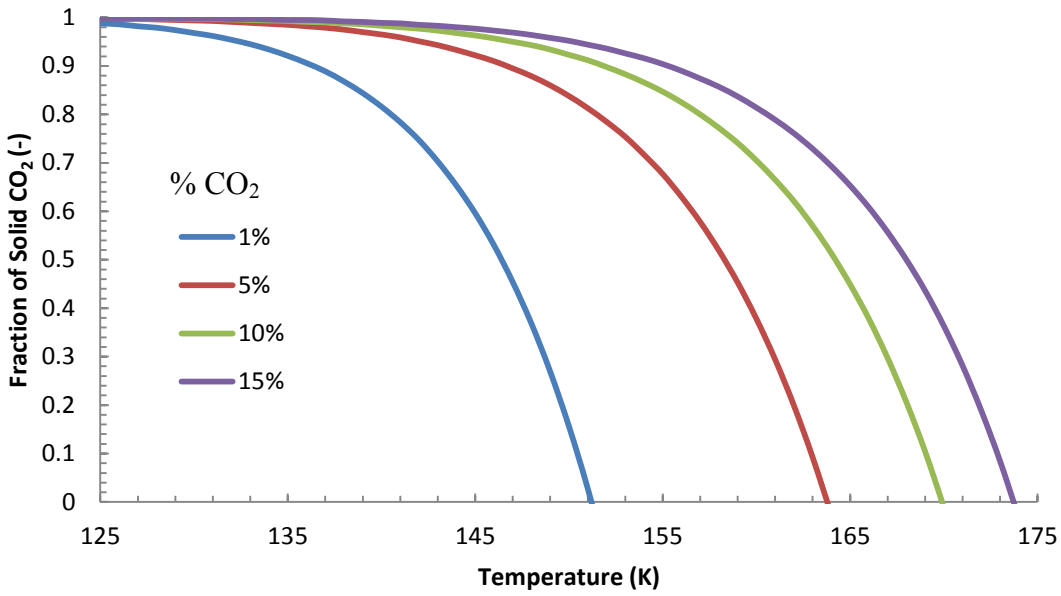

Figure 20: Percent solid CO_2 vs. temperature using a solid vapor equilibrium calculation

Figure 21 shows the percent CO_2 recovery vs. liquid temperature for all experiments conducted at 1 scfm of flue gas. The liquid temperatures shown and all future liquid temperatures were measured in the showerhead, at the top of the spray tower. Despite the scatter, the data show a clear trend, that the colder the liquid gets the better the capture from the gas. Regardless of the other operating conditions (liquid and gas flow rates) all data taken shows a similar trend. The solid lines show DTGT model predictions for the similar conditions assuming a liquid flow of 5 and 15 lpm. The model doesn't fit the data for 1 scfm as well as the equilibrium model, but on balance the improvement is large, as discussed in the next section.

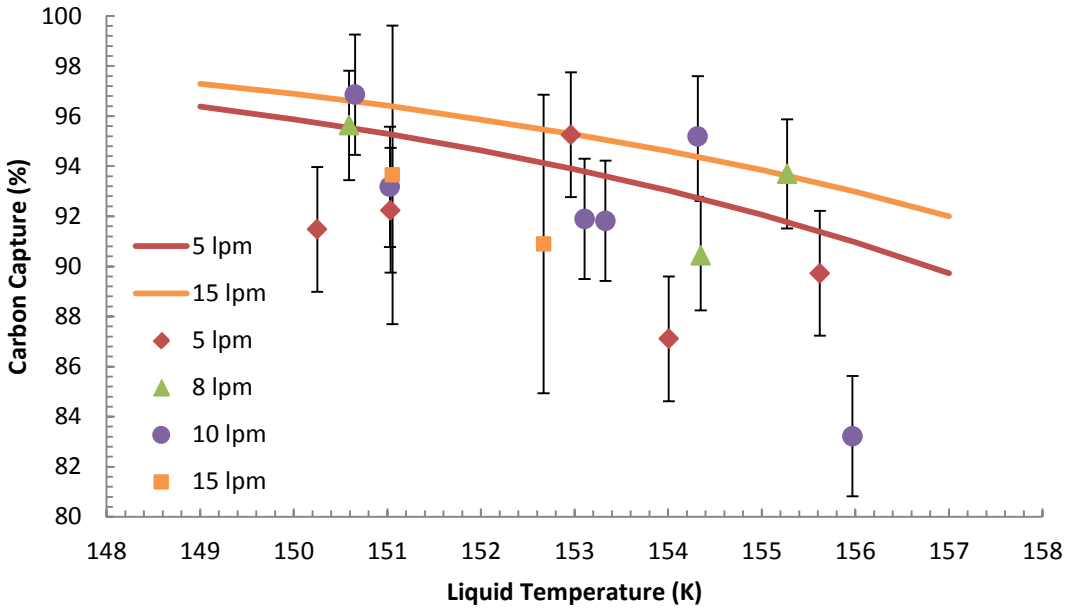

Figure 21: Percent carbon capture vs. liquid temperature for experiments done at 1 scfm gas flow and various liquid flow rates. The prediction lines are for 5 and 15 lpm liquid flow using the DTGT model.

5.2.2 Gas Flow Rate

For every set of conditions, there is an equilibrium CO_2 capture. Near-equilibrium CO_2 capture occurred in most of the experiment runs at high capture efficiencies. Thus, it took very large changes in operating conditions to perturb the system out of equilibrium. At gas flow rates greater than 1 scfm, lower than equilibrium values of CO_2 capture were measured. This trend appears clearly in Figure 22. The data for each gas flow rate appear, along with DTGT model predictions for 1, 1.5, 2, and 2.5 scfm gas flows. As the gas flow rate into the tower increases, the absolute amount of CO_2 in the tower increases. An increased amount of CO_2 in the tower means that increased cooling is needed to capture CO_2 at the same level. Cooling in the spray tower is supplied by the contact liquid, therefore if the gas flow rate increases without an increase in liquid flow rate, a drop in the CO_2 capture should be observed, unless still at equilibrium. The model predicts this, and the further away from equilibrium the better the model seems to predict.

That is not to say that the model doesn't predict equilibrium conditions well, but that the data taken around equilibrium conditions seems to have more scatter than the rest of the data.

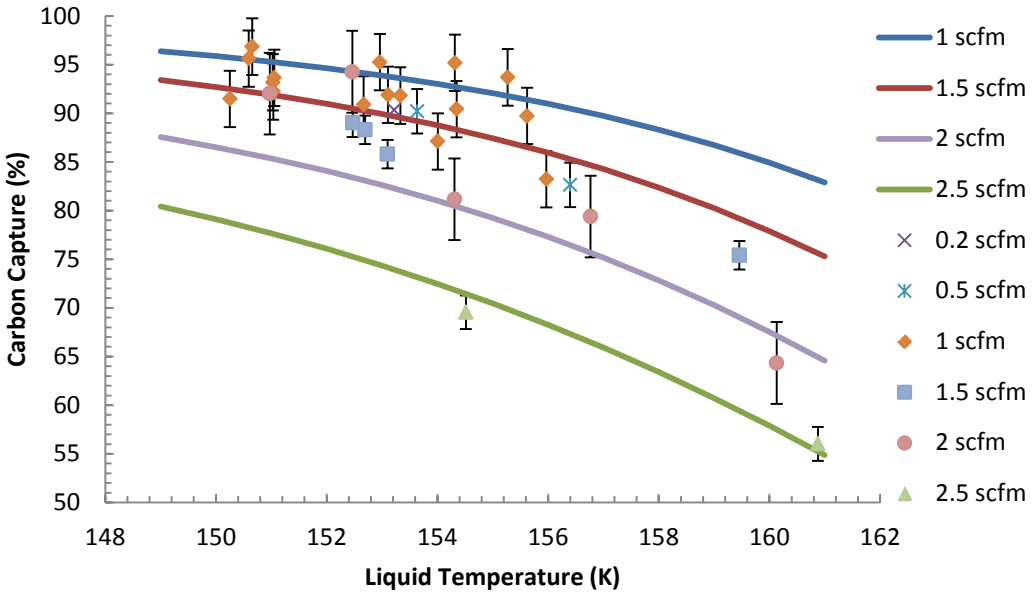

Figure 22: Percent carbon capture vs. liquid temperature vs. gas flow rate for all experiments, as well as DTGT model predictions for 1-2.5 scfm.

Unfortunately the data doesn't show the trend of increasing gas flow rate decreasing capture perfectly, because there wasn't total control of all experimental variables. The problem variable was with the liquid temperature. This was caused by the Polycold refrigeration system that was used. The system was not adjustable, once turned on it only cooled to its rated capacity. For some odd reason the refrigeration system cooled the liquid to a different temperature every day, even though everything else appeared to be identical. The cause of this was never investigated because it produced good temperature spread for experiments. Unfortunately, it also produced experimental results where more than one variable was changing at once.

5.2.3 Liquid Flow Rate

The same equilibrium explanation applies to liquid flow rates. A decrease in liquid flow rate while keeping the gas flow rate the same, will produce a lower CO_2 capture efficiency, unless the system is still in equilibrium. Figure 23 shows experimental data for percent carbon capture vs. liquid temperature sorted by liquid flow rates for data taken at 1 scfm, along with transport model predictions for 5, 8, and 10 lpm liquid flow. When sorted by liquid flow rate the model predictions don't look quite as good as they did before, but if you look at the error bars the predictions are still within almost every point's confidence interval. Figure 23 also shows that the system is in equilibrium after flow rates are greater than or equal to eight liters per minute, which as seen by the 8 and 10 lpm prediction lines being nearly identical. When all the data are viewed with the same predictions as before, the importance of the gas flow rate becomes obvious. It is also evident that the gas flow rate is a much larger factor in capture than liquid flow rate over the ranges varied here. Figure 24 shows all the data plotted, sorted by liquid flow rate, along with DTGT model predictions at 5 lpm liquid flow with 1 and 2.5 scfm gas flows. A somewhat linear relationship can be seen between flow rate and percent capture, but as explained in the previous section, changes in flow rate were also coupled with small changes in temperature, so the trend isn't perfectly smooth.

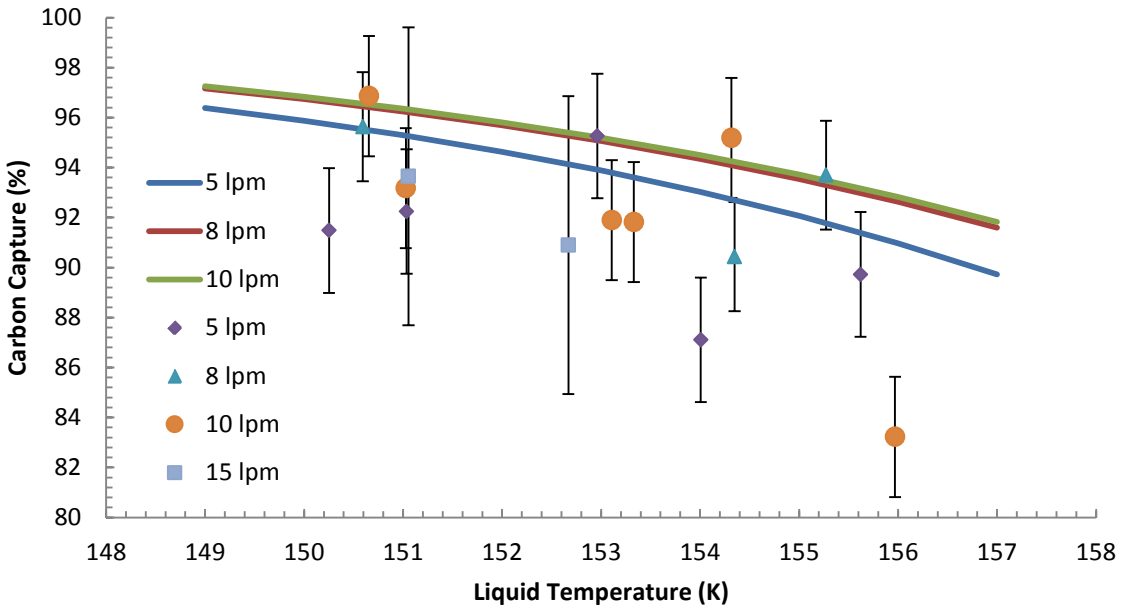

Figure 23: Percent carbon capture vs. liquid temperature vs. liquid flow rate at 1 scfm gas flow and various liquid flows, as well as DTGT model predictions for 5-10 lpm.

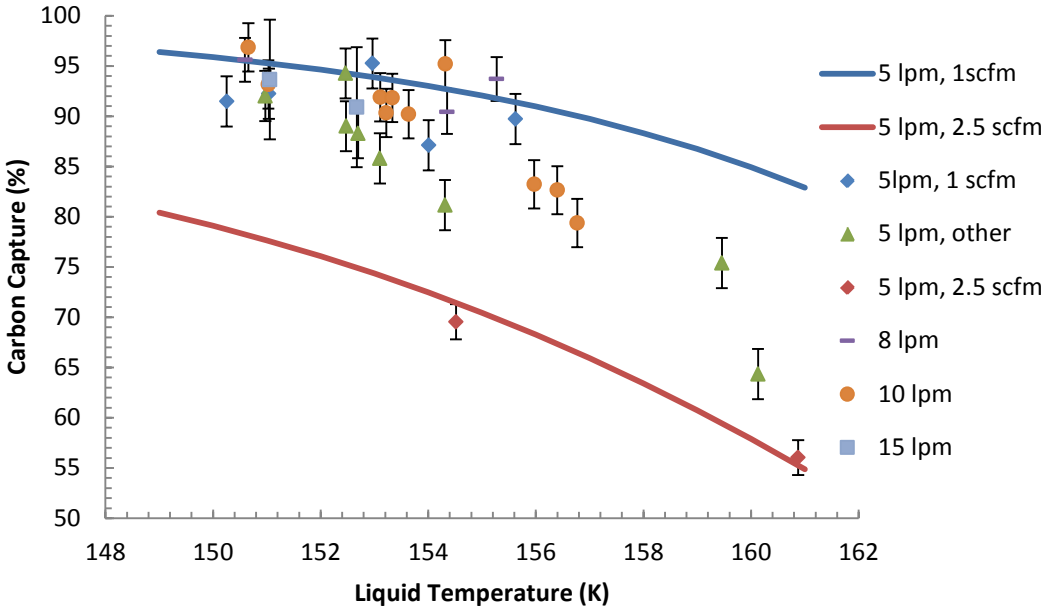

Figure 24: Percent carbon capture vs. liquid temperature vs. liquid flow rate for all data, as well as DTGT model predictions for 1 and 2.5 scfm.

5.2.4 Particle Size

All drop size experiments were done using the shot tower, due to the ease of using different sizes of shot, and because of the difficulty of changing and measuring the droplet size in the spray tower. Theory suggests that as the total surface area of particles increases the capture efficiency increases, thus smaller particles capture more CO_2. This occurs for two reasons. First, the primary method of heat transfer is via convection, which has a linear dependence on surface area. Second, desublimation requires a surface for crystals to form, so the greater the surface area the more available space for CO_2 crystals to grow.

Figure 25 displays experimental carbon capture data vs. position vs. shot diameter from the shot tower. The 2.16 mm old data points were measured using the first shot tower, and the 2.16 mm new data points were measured using the second shot tower. The data points for 2.16 mm old and new don't fall on the same line because of different operating conditions. The biggest difference between the operating conditions is the shot flow rate. The diameter of the second shot tower is twice as large as the diameter of the first spray tower, which allows a much higher total flow rate. A single data point is shown for 2 mm shot because experimentation was stopped using that shot size once it was confirmed that CO_2 capture was no different than when 2.16 mm shot was used. The said data point can be seen at (0.89, 99), below a point for 2.16 mm old shot.

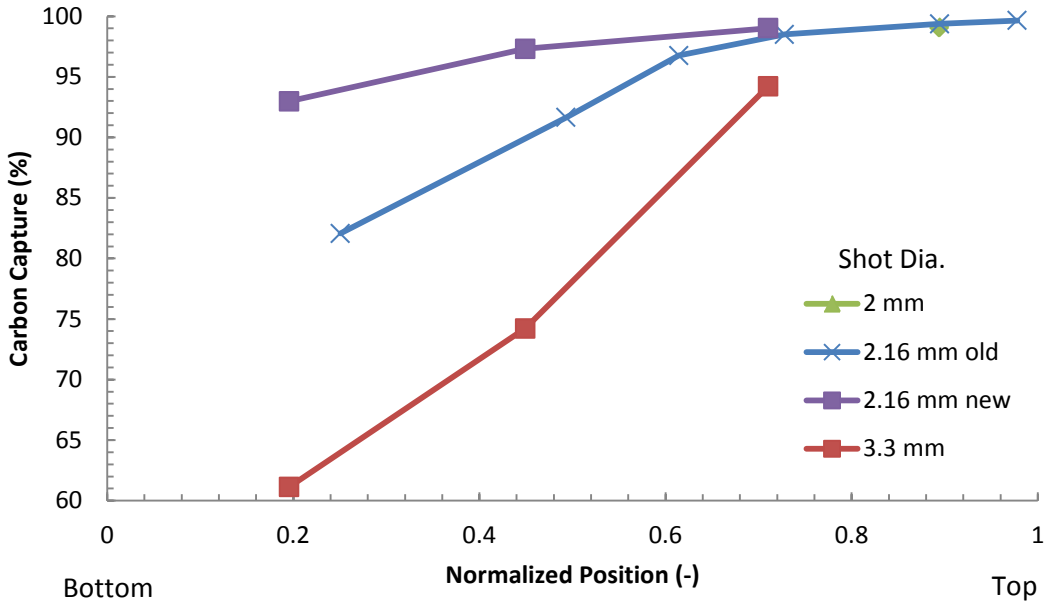

Figure 25: Percent carbon capture vs. position in shot tower for all shot sizes tested

Model predictions have not been calculated for experiments done with the shot tower, due to large uncertainties in shot temperature measurements. Despite not having predictions for actual shot tower conditions, the DTGT model can demonstrate the correct trend for changing particle size. Figure 26 displays predictions for percent carbon capture vs. position vs. particle size using the DTGT model. The conditions for the predictions are a 150 K liquid flow at 5 lpm, and 273.15 K gas flow at 1 scfm, with only the particle size changing. The particle sizes used for the predictions are in same range as the shot sizes used. Similar to the data in Figure 25, the predictions show smaller particle sizes capture more CO_2 and at a faster rate.

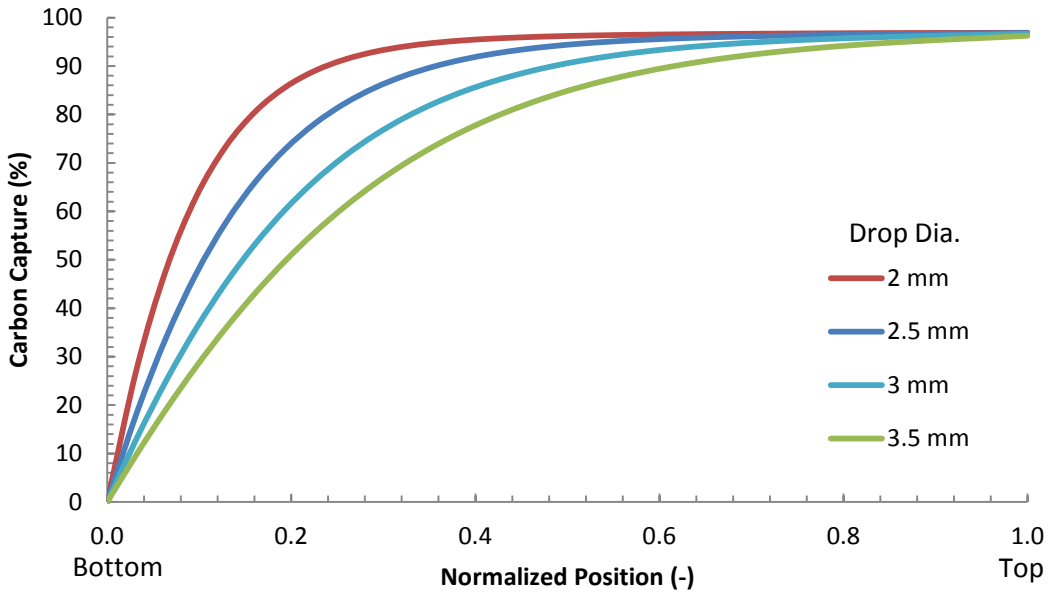

Figure 26: DTGT predictions for carbon capture vs. position vs. particle size

5.2.5 Tower Temperature Profile

The vacuum jacket surrounding the spray tower prevented temperature or gas composition profile measurements from being obtained from the tower during operation. Placing thermocouples throughout the side of the tower would have required penetrating the vacuum jacket, and sealing it at both sides. It was a difficult enough task to keep the vacuum from leaking without any penetrations, therefore the idea was quickly abandoned. Gas temperature measurements at the top and bottom of the tower provided the essential information needed for model validation, and while it is unknown what happened in between, the measurements follow the correct trend, namely that gas is progressively cooled as it moves up the tower, which is caused by the cold particles moving counter-currently.

Figure 27 shows the predicted gas temperature for the spray tower at steady state using the DTGT model. The conditions used for the prediction are 5 lpm liquid flow entering at 150 K

and 1 scfm gas flow entering at 273 K. These are the conditions of the base case for experimentation. Tower height or position has been normalized to 1, with zero being the top and one being the bottom. Figure 27 shows that the gas cools approximately 100 degrees, while the surface of the drop warms only by about 30 degrees. The exiting gas temperatures predicted by the model are much colder than actual measured exiting gas temperatures. This is because the gas thermocouples never reached steady state, presumably because of heat conduction along the thermocouple from the comparatively warm laboratory conditions. This is evident by the fact that the exiting gas temperature thermocouple kept cooling for the entire length of every run, without ever reaching a steady state.

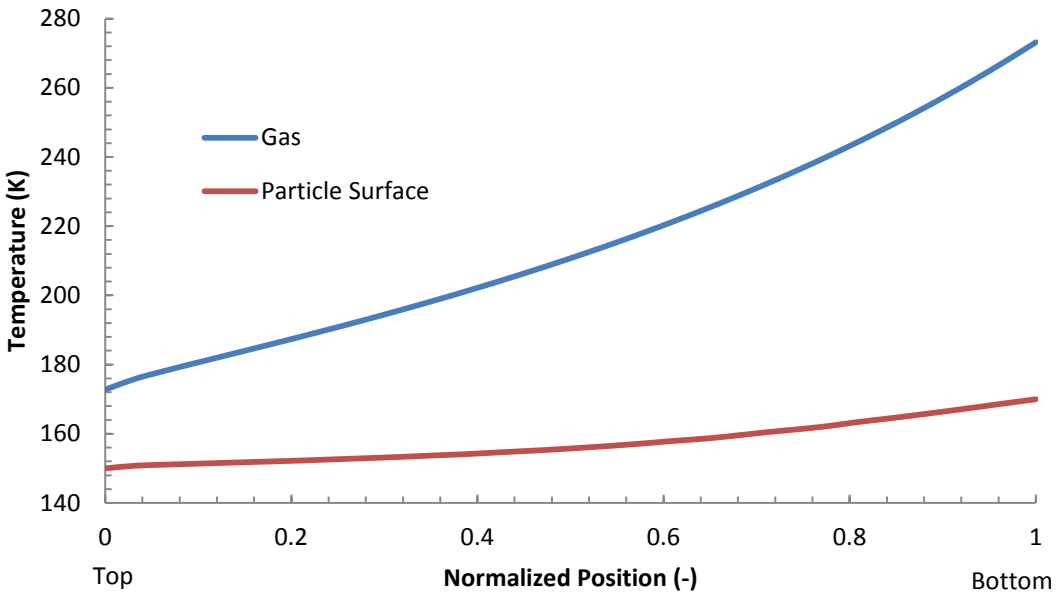

Figure 27: DTGT model predictions for gas and particle surface temperatures vs. position

Most of the previous results may be intuitive. It may be less intuitive to observe how much the temperature profile in these relatively small (nominal 3 mm) droplets affects the tower performance. This trend is the next section of this discussion, followed by a discussion of how

the predicted behavior can range from less capture than is predicted at equilibrium to more capture than is predicted in equilibrium.

5.2.6 Particle Temperature Profile

Previously it was mentioned that the equilibrium model diverges from the data at temperatures >157 K. The explanation for this deviation is that when the temperature of the contact liquid is near the temperature required to desublimate CO_2 that CO_2 will start to desublimate onto the surface of the drop, but then due to the heat of desublimation, the surface of the drop quickly heats up to a temperature above the desublimation temperature. This unexpected rise in temperature causes an unexpected decrease in carbon capture.

Due to experimental constraints, it was impossible to measure the temperature profile inside a droplet capturing CO_2, but the transport model predicts what the profile would be. Figure 28 shows what the predicted temperature profile would be for a drop after falling through the tower and capturing CO_2. The operating conditions for the prediction are once again 5 lpm liquid flow entering at 150 K and 1 scfm gas flow entering at 273 K. As can be seen by the graph, the center of the drop is still at the initial temperature, but the temperature at the surface of the drop has increased by almost 30 degrees. This increased surface temperature has a significant effect on the desublimation of CO_2. Temperature measurements on the spray tower were taken at the top and the bottom of the spray tower, before and after the liquid was sprayed. Thus, the thermocouples only reported bulk/average temperatures, making it impossible to see this surface temperature effect.

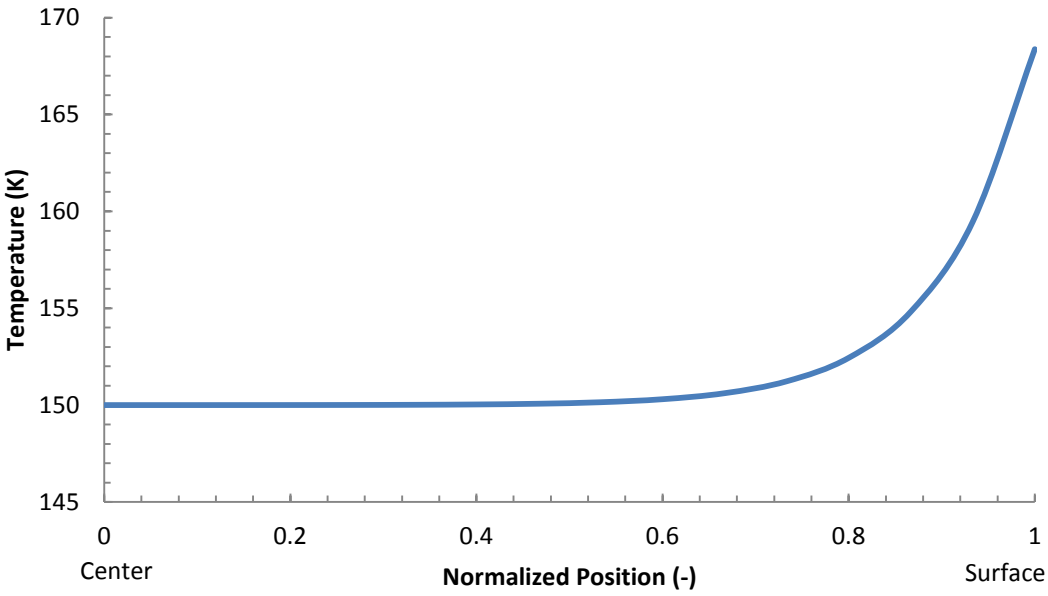

Figure 28: Typical DTGT model temperature profile for a drop at the bottom of the tower

5.3 Rigorous Capture Efficiencies Compared to Equilibrium

A comparison of the transport model predictions with the equilibrium model predictions shows that the transport model sometimes predicts higher and sometimes lower capture than equilibrium. This behavior is not completely intuitive and deserves some discussion. It is perhaps most intuitive that the transport model predicts less capture than equilibrium suggests. In these cases, the non-equilibrium (non-isothermal) temperature profile in the droplets raises the surface temperature to well above the average temperature. The droplet surface temperature can significantly exceed the average temperature, and the surface temperature determines the CO_2 desublimation rate. These are the conditions measured and predicted for most, but not all, of the data. If the droplet temperature profile did not exist (because of higher thermal conductivity or less viscous fluids leading the better mixing in the droplet), the surface temperature would be lower and capture efficiency would increase toward equilibrium values. Non-equilibrium

conditions in the gas phase composition can also lead to lower capture. If CO_2 diffusivities are very low, which they are at these low temperatures and for CO_2 in general relative to other gases, then desublimation decreases because of slow gas transport.

At some conditions, the droplets capture more CO_2 than equilibrium suggests. In these cases, the droplets are collecting CO_2 in the thermal boundary layer around the droplets even though the number of droplets is too small to lower the bulk gas temperature significantly. An extreme case would be a single cold droplet dropping through an effectively infinite amount of room-temperature flue gas. The equilibrium prediction would say the droplet should warm to room temperature, which it will eventually do. However, it will initially desublimate CO_2 in its immediate surroundings since it can cool the finite amount of flue gas in its thermal boundary layer to desublimation temperatures before it warms above its frost point. As in the previous case, if conditions were closer to equilibrium by virtue of higher gas thermal conductivity or smaller droplets with smaller boundary layers and less difference in droplet and gas temperature, the CO_2 capture would approach equilibrium. However, in this case, equilibrium is lower capture efficiency, not higher capture efficiency as is the case described previously. In this prediction, significant thermal non-equilibrium conditions in the droplets leads to a decrease in capture efficiency while significant thermal non-equilibrium conditions in the gas phase leads to higher capture efficiency.

The transport model predicts both effects, as seen by the transport model parity plot predictions crossing the equilibrium model parity plot predictions.

5.4 Variable Sensitivity

This work demonstrates the order of importance for the variables tested in a desublimating spray tower, which is as follows

1. Liquid Temperature
2. Drop Size
3. Gas Flow Rate
4. Liquid Flow Rate

Liquid temperature was shown to be the most important variable which was expected. This is due to the fact that heat transport has a greater influence than mass transport in this case, and heat transport is linearly dependent on the temperature gradient. Larger gradients lead to more cooling. Particle size came in second because it is also directly related to heat transfer. This relation is due to the fact that surface area is a function of particle size, and heat transport is linearly dependent on the surface area as well. The next two variables are flow rates and while they do affect heat transport they have a smaller effect, primarily they affect mass transport. Gas flow rate was shown to be more important than liquid flow rate because it represents the amount of cooling required, whereas the liquid flow rate represents the amount of cooling available, and at most of the conditions tested the cooling required was the limiting factor.

6 CONCULSION

The viability of a desublimating spray tower has been demonstrated by a shot tower and a spray tower that both achieved greater than 95% CO_2 capture at optimized operating conditions. This research documents the construction and operation of five such towers with increasing performance. Experimental lab- and bench-scale results illustrating trends in tower performance with respect to the liquid properties of temperature, flowrate, and droplet size and the gas properties of temperature and flow rate. The desublimating spray tower achieves arbitrarily high capture efficiency, with well over 95% capture included in these results. It also runs continuously with no oscillatory changes in pressure or temperature. Based on a typical coal flue gas, the experimentally observed and theoretically predicted capture depends on

1. Liquid temperature, with capture efficiencies ranging from 55 – 96 % as temperatures range from 150 – 160 K
2. Drop size, with capture efficiencies ranging from 94 – 100 % as particles range from 2 – 3.33 mm
3. Gas flow rate, with capture efficiencies ranging from 55 – 96 % as gas flow rates range from 0.2 – 2.5 scfm
4. Liquid flow rate, with capture efficiencies ranging from 83 – 96 % as liquid flow rates range from 5 – 15 lpm

The dependence of tower performance on the droplet temperature profile, and the observed and predicted behavior of the tower collecting both more and less CO_2 than predicted by a local equilibrium model represent unanticipated and potentially non-intuitive results. An equilibrium model was developed that accurately predicts capture for much of the data collected, meaning that most of the conditions were near local equilibrium conditions. The model deviated from the data at warm liquid temperatures by predicting higher than measured capture. Because of this deviant behavior a more rigorous transport model, DTGT model, was developed. The DTGT model simultaneously solves the Navier-Stokes equations for energy, mass, and momentum. The DTGT model predicts capture for the entire range of data within ± 2.31 % error. This model provides tower design and scaling capabilities validated by the bench-scale data.

REFERNCES

(2007). Massachusetts v. EPA. U.S. 549.

(CADC 2012). Coalition for Responsible Regulation, Inc. et al. v. EPA. **No. 09-1322**.

ACENT-Labs. (2013). "Carbon Capture and Storage - Gas Separation." Retrieved May 30, 2013, from http://acentlabs.com/business-areas/carbon-capture/.

ARPA-E. (2013). "Supersonic Technology for CO2 Capture: A High Efficency Inertial CO2 Extraction System." Retrieved May 30, 2013, from http://arpa-e.energy.gov/?q=arpa-e-projects/supersonic-technology-co2-capture.

Baxter, L., A. Baxter and S. Burt (2009). "Cryogenic CO2 capture to control climate change emissions." Int. Tech. Conf. Clean Coal Fuel Syst. **34**(Copyright (C) 2012 American Chemical Society (ACS). All Rights Reserved.): 705-717.

Baxter, L. L. (2011). Carbon Dioxide Capture From Flue Gas. **US 2011/0226010A1**

Baxter, L. L. and C. S. Bence (2012). Systems and Methods for Separating Condensable Vapors From Gases By Direct-Contact Heat Exchange. **US 2012/01533514 A1**.

Baxter, L. L., S. Burt and A. Baxter (2009). Cryogenic Carbon Capture. Environmental Management and Engineering 2009; International Association of Science and Technology for Development, Banff, Canada, ACTA Press.

Bence, C., D. W. James and L. L. Baxter (2010). Overcoming Heat Exchanger Issues within a Cryogenic CO2 Capture Process. AIChE 2010 Annual Meeting. Salt Lake City, UT, AIChE.

Ciferno, J. P., J. L. Litnski and S. I. Plasynski (2010). DOE/NETL Carbon Dioxide Capture and Storage RD&D Roadmap, DOE/NETL.

Ciferno, J. P. and J. J. Marano (2008). Novel integration of gas separation membranes for CO2 Capture from IGCC power plants. 2008 AIChE Spring National Meeting, Conference, April 6, 2008 - April 10, 2008. New Orleans, LA.

Clodic, D. and M. Younes (2002). Method and system for recovery of carbon dioxide from flue gases by desublimation for its storage, Armines, Fr. . 64 pp.

Clodic, D. and M. Younes (2003). A new method for CO2 capture: frosting CO2 at atmospheric pressure, Elsevier Ltd.

Clodic, D., M. Younes and A. A. Bill (2005). CO2 capture by anti-sublimation Thermo-economic process evaluation. 4th Annual Conference on Carbon Capture & Sequestration. Alexandria, Virgina.

Court, B., T. R. Elliot, J. Dammel, T. A. Buscheck, J. Rohmer and M. A. Celia (2012). "Promising synergies to address water, sequestration, legal, and public acceptance issues associated with large-scale implementation of CO2 sequestration." Mitigation and Adaptation Strategies for Global Change **17**(6): 569-599.

Davison, J. and K. Thambimuthu (2009). "An overview of technologies and costs of carbon dioxide capture in power generation." Proceedings of the Institution of Mechanical Engineers, Part A: Journal of Power and Energy **223**(3): 201-212.

Ebner, A. D., M. L. Gray, N. G. Chisholm, Q. T. Black, D. D. Mumford, M. A. Nicholson and J. A. Ritter (2011). "Suitability of a Solid Amine Sorbent for CO2 Capture by Pressure Swing Adsorption." Industrial & Engineering Chemistry Research **50**(Copyright (C) 2012 American Chemical Society (ACS). All Rights Reserved.): 5634-5641.

Ebner, A. D. and J. A. Ritter (2009). "State-of-the-art adsorption and membrane separation processes for carbon dioxide production from carbon dioxide emitting industries." Sep. Sci. Technol. **44**(Copyright (C) 2012 American Chemical Society (ACS). All Rights Reserved.): 1273-1421.

Eide, L. I., M. Anheden, A. Lyngfelt, C. Abanades, M. Younes, D. Clodic, A. A. Bill, P. H. M. Feron, A. Rojey and F. Giroudiere (2005). "Novel carbon dioxide capture processes." Oil Gas Sci. Technol **60**(Copyright (C) 2012 American Chemical Society (ACS). All Rights Reserved.): 497-508.

EPA. (2011). "Climate Change - Greenhouse Gase Emissions: Carbon Dioxide." Retrieved April 3, 2012, from http://www.epa.gov/climatechange/emissions/co2.html.

EPA. (2012). "Carbon Pollution Standard for New Power Plants - Basic Information." Retrieved April 10, 2013, from http://epa.gov/carbonpollutionstandard/basic.html.

EPA. (2012). "Mercury and Air Toxics Standards." Retrieved June 6, 2013, from http://www.epa.gov/airquality/powerplanttoxics/index.html.

Hoeger, C., C. Bence, S. Burt, A. Baxter and L. L. Baxter (2010). Cryogenic CO2 capture for improved efficiency at reduced cost. 2010 AIChE Annual Meeting. Salt Lake City, UT, AIChE.

Hu, J. Y., W. Dai, E. C. Luo, X. T. Wang and Y. Huang (2010). "Development of high efficiency Stirling-type pulse tube cryocoolers." Cryogenics **50**(9): 603-607.

Jackson, L. P. (2012). Proposed Carbon Pollution Standard for New Power Plants. (EPA-HQ-OAR-2011-0660. EPA.

James, D. W. (2011). FALLING DROP CO2 DEPOSITION (DESUBLIMATION) HEAT EXCHANGER FOR THE CRYOGENIC CARBON CAPTURE. MS, BYU.

Larsen, R., C. Fox, B. Meldrum and L. L. Baxter (2010). Cryogenic pollutant balances extended abstract, American Institute of Chemical Engineers.

Larsen, R., C. Fox, B. Meldrum, J. Hartvitssen and L. Baxter (2010). "Cryogenic pollutant removal." Int. Tech. Conf. Clean Coal Fuel Syst. **35**(Copyright (C) 2012 American Chemical Society (ACS). All Rights Reserved.): 1468-1477.

Le Treut, H., R. Somerville, U. Cubasch, Y. Ding, C. Mauritzen, A. Makssit, T. Peterson and M. Prather (2007). Historical Overview of Climate Change. In: Climate Change 2007: The Physical Science Basis. Contribution of Working Group I to the Fourth Assessment Report of the Intergovernmental Panel on Climate Change [Solomon, S., D. Qin, M. Manning, Z. Chen, M. Marquis, K.B. Averyt, M. Tignor and H.L. Miller (eds.)]. Cambridge, United Kingdom and New York, NY, USA, Cambridge University Press.

Obama, B. (2013). "President Obama's Plan to Fight Climate Change." Retrieved June 28, 2013, from http://www.whitehouse.gov/share/climate-action-plan.

Orr, F. M. (2009). "CO2 capture and storage: are we ready?" Energy & Enviromental Sciences **2**(5): 449-458.

Perrotin, T. and D. Clodic (2005). CO2 gas cooler modeling and optimization, International Institute of Refrigeration.

Perry, R. H., D. W. Green and J. O. Maloney, Eds. (2012). Perry's Chemical Engineering Handbook. USA, McGraw-Hill, Inc.

Polezhaev, Y. V. and I. V. Chircov (2011) "Drag Coefficent."

Rao, A. B. and E. S. Rubin (2002). "A technical, economic, and environmental assessment of amine-based CO2 capture technology for power plant greenhouse gas control." Environmental Science & Technology **36**(20): 4467-4475.

Rubin, E. S. and H. B. Zhai (2012). "The Cost of Carbon Capture and Storage for Natural Gas Combined Cycle Power Plants." Environmental Science & Technology **46**(6): 3076-3084.

Schach, M.-O., B. Oyarzun, H. Schramm, R. Schneider and J.-U. Repke (2011). "Feasibility study of CO2 capture by anti-sublimation." Energy Procedia **4**(Copyright (C) 2012 American Chemical Society (ACS). All Rights Reserved.): 1403-1410.

Schreiber, A., P. Zapp and W. Kuckshinrichs (2009). "Environmental assessment of German electricity generation from coal-fired power plants with amine-based carbon capture." International Journal of Life Cycle Assessment **14**(6): 547-559.

Siemens. (2012). "Combined cycle power plants." Retrieved August 10, 2012, from http://www.siemens.com/sustainability/en/environmental-portfolio/products-solutions/fossil-power-generation/combined-cycle-power-plants.htm.

Siemens. (2012). "Simple cycle power plants." Retrieved August 10, 2012, from http://www.siemens.com/sustainability/en/environmental-portfolio/products-solutions/fossil-power-generation/simple-cycle-power-plants.htm.

Song, C.-F., Y. Kitamura, S.-H. Li and W.-Z. Jiang (2013). "Analysis of CO2 frost formation properties in cryogenic capture process." International Journal of Greenhouse Gas Control **13**: 26-33.

Song, C. F., Y. Kitamura and S. H. Li (2012). "Evaluation of Stirling cooler system for cryogenic CO2 capture." Applied Energy **98**: 491-501.

Song, C. F., Y. Kitamura, S. H. Li and W. Z. Jiang (2012). "Parametric Analysis of a Novel Cryogenic CO2 Capture System Based on Stirling Coolers." Environmental Science & Technology **46**(22): 12735-12741.

Song, C. F., Y. Kitamura, S. H. Li and K. Ogasawara (2012). "Design of a cryogenic CO2 capture system based on Stirling coolers." International Journal of Greenhouse Gas Control **7**: 107-114.

Tans, P. (2012). "Trends in Atmospheric Carbon Dioxide." Retrieved April 3, 2012, from http://www.esrl.noaa.gov/gmd/ccgg/trends/.

Toftegaard, M. B., J. Brix, P. A. Jensen, P. Glarborg and A. D. Jensen (2010). "Oxy-fuel combustion of solid fuels." Progress in Energy and Combustion Science **36**(5): 581-625.

Tuinier, M. J., M. van Sint Annaland, G. J. Kramer and J. A. M. Kuipers (2010). "Cryogenic CO2 capture using dynamically operated packed beds." Chemical Engineering Science **65**(1): 114-119.

Tuinier, M. J., M. Van Sint Annaland and J. A. M. Kuipers (2011). "A novel process for cryogenic CO2 capture using dynamically operated packed beds-An experimental and numerical study." International Journal of Greenhouse Gas Control **5**(4): 694-701.

Wall, T. F. (2007). "Combustion processes for carbon capture." Proceedings of the Combustion Institute **31**: 31-47.

7 APPENDIX

7.1 Sylvia LabVIEW Program

7.1.1 Front Panel

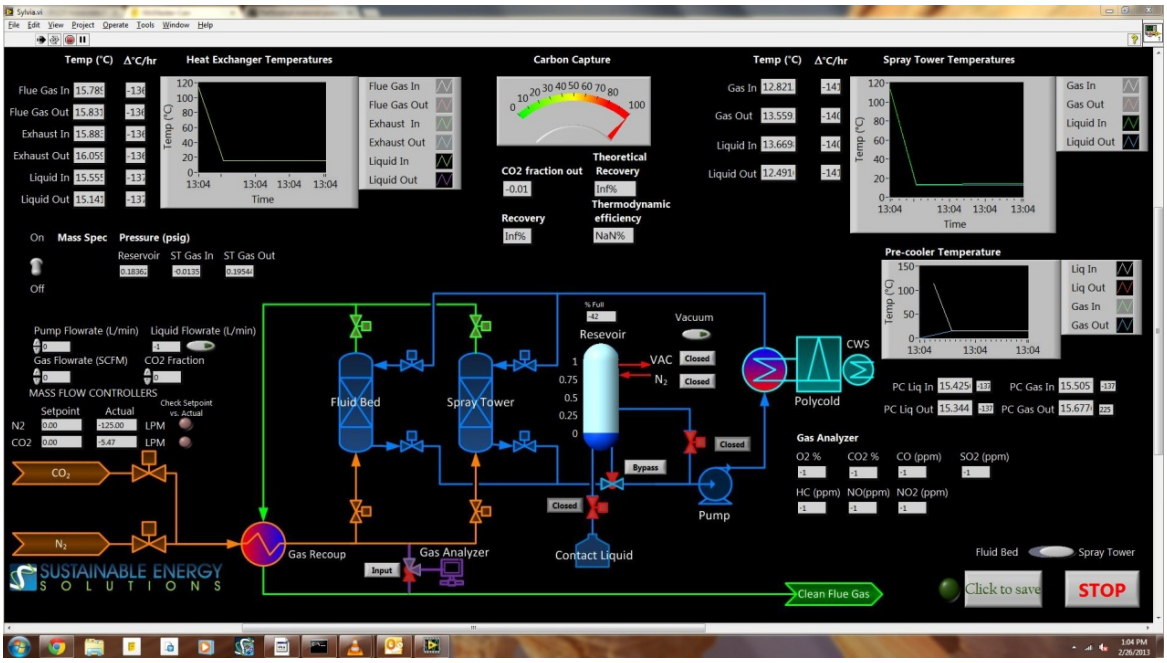

The front panel includes buttons and controls for all of the equipment on Sylvia. Numerical and graphical indicators are also included for all measurements.

7.1.2 Thermocouples and Pressure Transducers

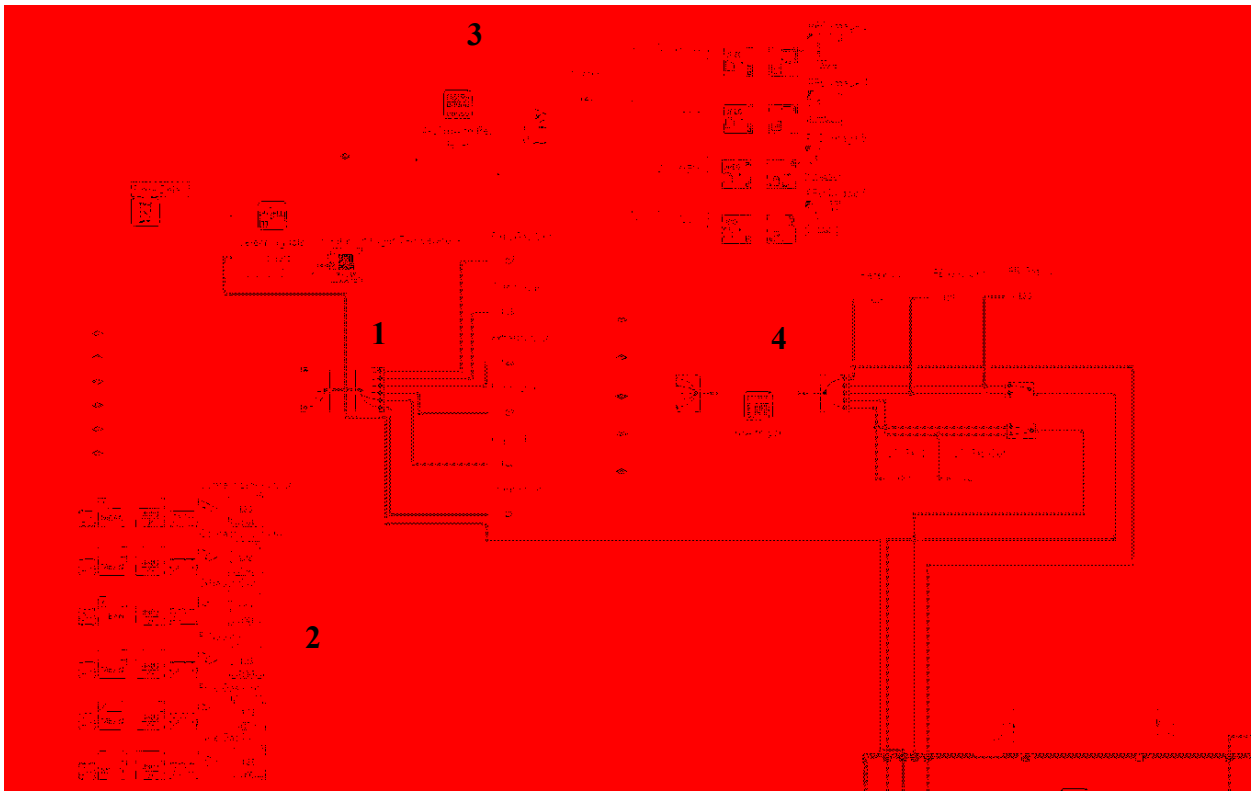

In region one thermocouple signals are read in, and then bundled together and sent multiple places. The wire going up goes to a function to reorder the signals, and then it goes to a graph. The down wire passes through a loop which then goes into a data file. The right wire is unbundled, and each signal is sent to a numerical indicator. In region two formulas are used to calculate the average rate of change through the last 20 thermocouple measurements, and then display it in an indicator. In region three the reservoir level meter signal is read in and converted to a percentage, then output to a numerical and a visual indicator. In region four pressure transducer signals are read in, converted to psi, then output to numerical indicators as well as being sent to the data file.

7.1.3 Mass Flow Controllers

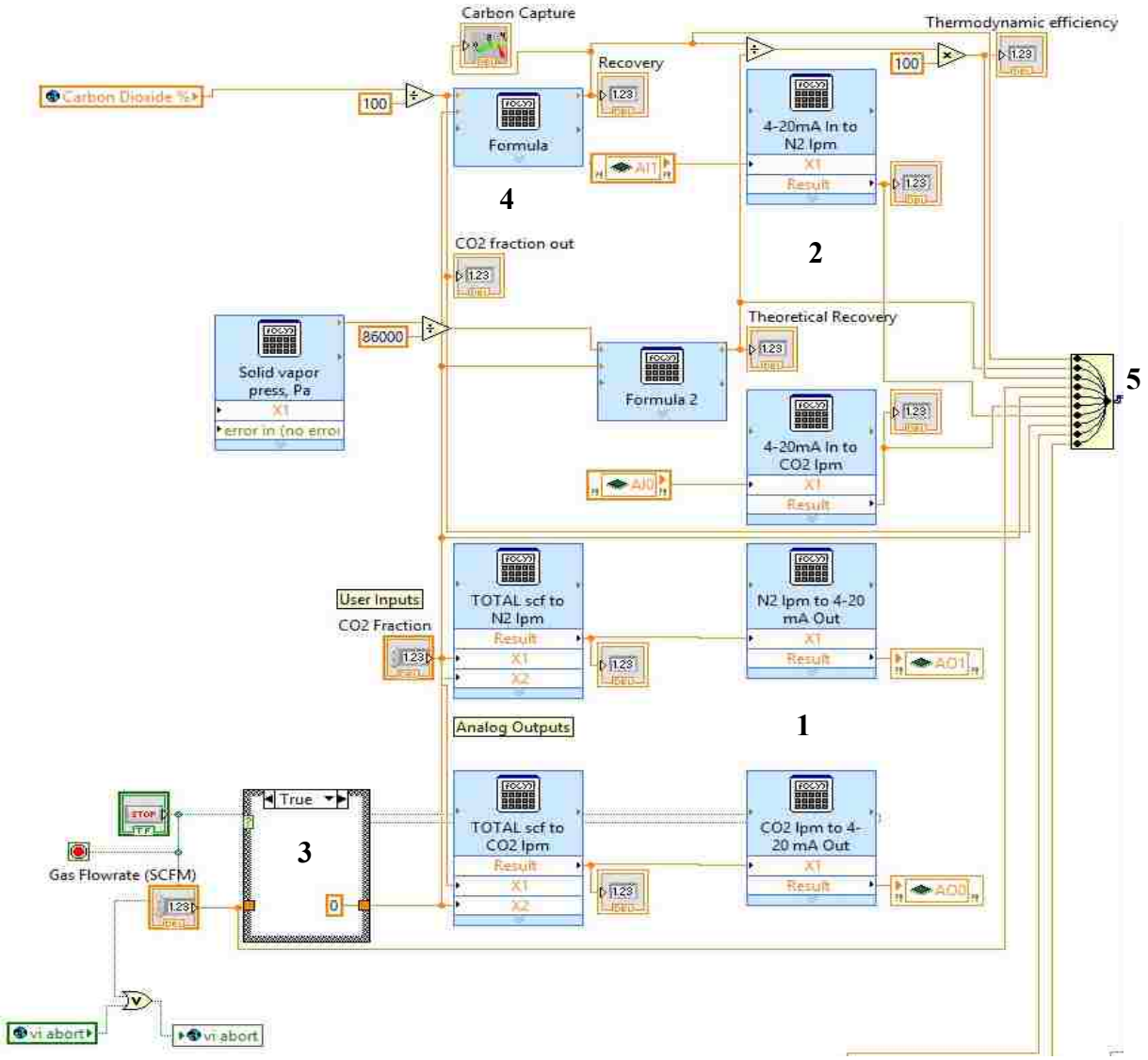

In region one the variables gas flow rate and CO_2 fraction are converted to lpm of flow for CO_2 and N_2. The signals are then converted to mA signals, and sent to the individual mass flow controllers. In region two feedback signals are read in from the MFCs, converted from mA to lpm, and then output to an indicator. In region three the gas flow rate variable is passed through a loop that changes the variable to zero when the stop button is pushed on the front panel. This prevents the MFCs from flowing gas after the program has been stopped. In region

four the percent carbon capture is calculated, and output to a numerical and visual indicator. In region five all signals are bundled and sent to the data file.

7.1.4 Valves

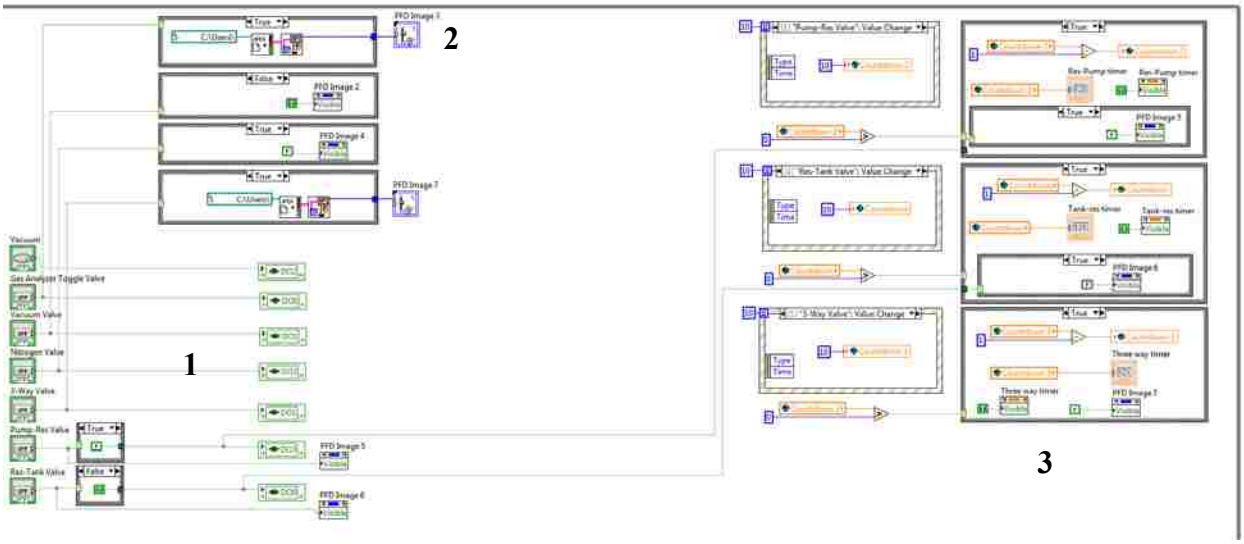

In region one, switches are wired to outputs in the DAQ that control each valve. Toggling a valve in region one triggers a different graphic to become visible on the PFD on the front panel, which is done in region two. At the same time a countdown timer is activated and displayed on the front panel, which counts down the time it takes for the valve to switch, which is done in region three.

7.1.5 Pump, Gas Analyzer, and Flow Meter

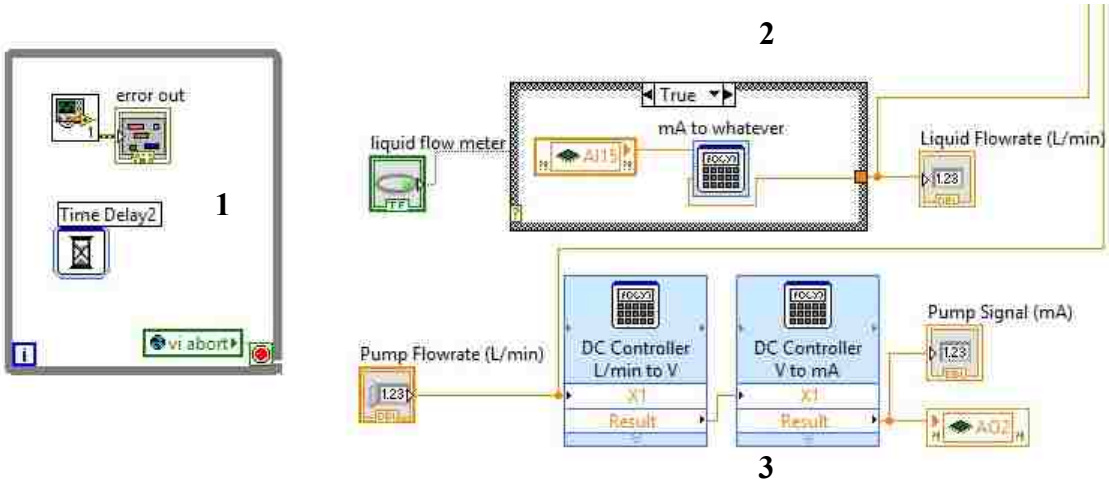

In region one, a sub vi used to read values from a gas analyzer. The output from the gas analyzer is stored as global variables, which means that the main vi and all sub vis need to be part of the same project. In region two a signal from a liquid flow meter is read in, and then converted to lpm, then output to a numerical indicator. All of that is inside a loop which is controlled to by a switch, so that the output can be turned off when the flow meter isn't connected. In region three the pump flow rate variable is converted from lpm to V to mA, and then sent to the module that is connected to the pump controller.

7.1.6 Write to Measurement and Global Variables

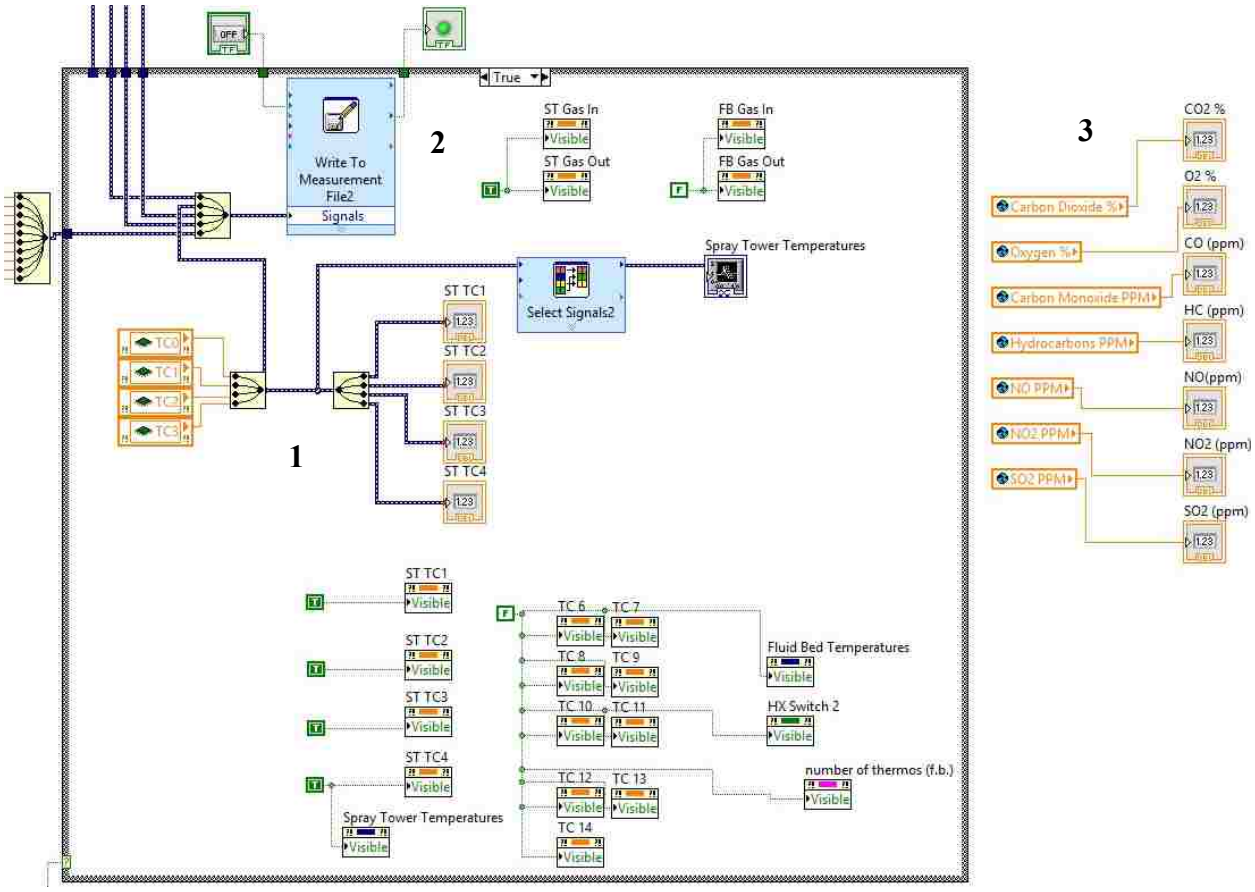

In region one, thermocouples are read in, output to indicators, graphed, and sent to the data file, almost identical to the other set of thermocouples shown. Region two is the data file function, which has data coming from every other part of the program that is saved in a data file. The data file is controlled with a switch, so it only logs data when it switch is on. The data file is also connected to a visual indicator, so you can see when data is logging. In region three global variables are read in for gas concentrations measured by the gas analyzer, and then output to numerical indicators.

7.2 Spray Tower Data

Date	Point	Gas In (°C)	Gas Out (°C)	Liq In (°C)	Liq Out (°C)	Reservoir (psi)	ST Gas In (psi)	ST Gas Out (psi)	Gas Flowrate (SCFM)	CO2 Fraction	Liquid flow (LPM)	Recovery
17-Sep	1	0.66	-50.32	-122.11	-117.06	0.18	9.61	8.55	1	0.15	5	92.24
	2	1.94	-62.66	-122.56	-117.44	0.18	8.07	6.87	1	0.15	8	95.63
	3	2.23	-69.44	-122.50	-117.79	0.18	8.74	7.59	1	0.15	10	96.86
18-Sep	4	0.35	-26.44	-117.53	-112.39	0.18	10.61	9.80	1	0.15	5	89.72
	5	1.29	-50.28	-117.88	-114.43	0.18	10.45	9.61	1	0.15	8	93.69
	6	1.77	-58.58	-118.83	-115.70	0.18	8.84	7.85	1	0.15	10	95.19
	7	2.20	-62.24	-120.19	-116.92	0.18	6.58	5.37	1	0.15	5	95.26
19-Sep	8	2.54	-12.39	-119.14	-113.66	0.18	10.77	9.69	1	0.15	5	87.11
	9	3.85	-39.63	-118.80	-113.72	0.18	11.51	10.56	1	0.15	8	90.43
	10	4.66	-52.79	-120.04	-113.39	0.18	11.12	10.18	1	0.15	10	91.90
	11	5.12	-58.64	-120.48	-112.32	0.18	9.71	8.68	1	0.15	15	90.90
23-Oct	12	-2.72	-31.41	-122.90	-119.22	0.18	10.48	10.18	1	0.15	5	91.48
	13	-5.36	-47.83	-122.12	-118.08	0.18	8.87	8.45	1	0.15	10	93.18
	14	-6.02	-53.52	-122.10	-117.86	0.18	6.67	6.05	1	0.15	15	93.65
	15	-5.76	-72.13	-122.18	-116.12	0.18	11.75	8.58	2	0.15	5	92.02
30-Oct	16	11.59	-59.97	-120.68	-113.97	0.18	13.25	11.08	1.5	0.15	5	89.02
7-Nov	17	-1.65	-29.71	-120.46	-112.72	0.18	15.42	13.48	1.5	0.15	5	88.30
	18	-0.30	-56.63	-118.84	-109.73	0.18	19.37	16.23	2	0.15	5	81.16
	19	1.20	-75.02	-118.64	-105.54	0.18	19.26	13.83	2.5	0.15	5	69.55
8-Nov	20	0.51	-39.59	-113.69	-107.09	0.18	16.74	15.19	1.5	0.15	5	75.40
	21	-0.50	-58.17	-113.02	-106.47	0.18	13.47	9.69	2	0.15	5	64.34
	22	-0.39	-71.23	-112.28	-104.42	0.18	13.39	6.65	2.5	0.15	5	56.03
12-Nov	23	-33.34	-40.02	-120.05	-114.62	0.19	6.50	5.14	1.5	0.15	5	85.80
13-Nov	24	-36.76	-31.55	-120.69	-113.45	0.19	16.25	15.92	2	0.15	5	94.27
27-Nov	25	-1.83	-50.78	-119.82	-115.70	0.18	10.20	10.07	1	0.15	10	91.82
	26	-3.14	-56.47	-119.52	-115.85	0.18	3.47	3.87	0.5	0.15	10	90.20
	27	-5.74	-55.30	-119.93	-116.97	0.18	0.62	1.38	0.2	0.15	10	90.34
4-Dec	28	-6.55	-62.04	-117.18	-111.78	0.18	5.33	4.94	1	0.15	10	83.22
	29	-7.38	-60.02	-116.75	-112.10	0.18	1.61	2.12	0.5	0.15	10	82.64
	30	-5.98	-66.42	-116.38	-108.92	0.18	13.30	10.38	2	0.15	10	79.39

7.3 Spray Tower Statistical Analysis

Point	Liquid In	Gas	Liquid	Recovery	Pred Rec	Diff	Std Dev	n	95% conf	Avg Error	Avg	Min	Max
27	153.22	0.2	10	90.34	92.17	-1.83							
26	153.63	0.5	10	90.20	93.10	-2.90	1.59	2	2.29	2.29	86.42	84.13	86.42
29	156.40	0.5	10	82.64	88.71	-6.07							
1	151.04	1	5	92.24	95.25	-3.00	2.81	5	2.57	2.90	91.16	88.59	91.16
4	155.62	1	5	89.72	91.71	-1.99							
7	152.96	1	5	95.26	93.05	2.21							
8	154.01	1	5	87.11	93.24	-6.14							
12	150.25	1	5	91.48	95.93	-4.45							
2	150.59	1	8	95.63	96.16	-0.53	1.85	3	2.18		93.25	91.07	93.25
5	155.27	1	8	93.69	93.52	0.18							
9	154.35	1	8	90.43	94.49	-4.05							
3	150.65	1	10	96.86	96.35	0.51	3.02	6	2.52		92.03	89.51	92.03
6	154.32	1	10	95.19	94.01	1.17							
10	153.11	1	10	91.90	95.40	-3.51							
13	151.03	1	10	93.18	96.24	-3.06							
25	153.33	1	10	91.82	95.17	-3.35							
28	155.97	1	10	83.22	91.23	-8.01							
11	152.67	1	15	90.90	95.44	-4.54	4.13	2	5.96		92.28	86.32	92.28
14	151.05	1	15	93.65	89.94	3.72							
16	152.47	1.5	5	89.02	89.94	-0.92	1.43	4	1.46	1.46	84.63	83.17	84.63
17	152.69	1.5	5	88.30	90.65	-2.35							
20	159.46	1.5	5	75.40	80.02	-4.63							
23	153.10	1.5	5	85.80	89.70	-3.89							
15	150.97	2	5	92.02	85.66	6.37	4.11	4	4.20	4.20	82.95	78.75	82.95
18	154.31	2	5	81.16	80.41	0.74							
21	160.13	2	5	64.34	66.94	-2.60							
24	152.46	2	5	94.27	86.82	7.45							
30	156.77	2	10	79.39	91.01	-11.63							
19	154.51	2.5	5	69.55	70.87	-1.32	1.20	2	1.74	1.74	62.79	61.05	62.79
22	160.87	2.5	5	56.03	54.94	1.09							
							Total	28	**Avg**	2.75			

7.4 Shot Tower Data

	Shot Dia	Pos	Pos (in)	Shot Flow (kg/s)	Gas Flow (lpm)	Res T1 (K)	Shot inlet T2 (K)	T4 (K)	T5 (K)	T7 (K)	T8 (K)	T9 (K)	T10 (K)	T11 (K)	T13 (K)	Gas In (K)	%CO2	Capture
new	0.085	Bottom	27	0.1844	2.1	126.98	178.94	294.99	289.52	290.03	288.28	295.84	286.07	294.79	296.65	176.73	1.13	92.98
	0.085	Bottom	27	0.1844	2.1	127.69	179.63	294.75	288.89	290.08	289.91	295.49	288.86	294.43	296.06	177.77	1.13	92.98
	0.085	Middle	62	0.1844	2.1	168.36	174.78	295.76	285.35	288.15	282.64	296.17	277.99	295.70	296.23	177.05	0.44	97.34
	0.085	Middle	62	0.1844	2.1	128.85	188.58	294.09	289.24	289.41	286.01	294.95	289.92	293.73	296.07	176.72	0.43	97.29
	0.085	Top	98	0.1844	2.1	204.44	281.33	295.87	290.24	287.23	288.79	296.95	290.40	295.93	297.02	177.85	0.15	99.08
	0.085	Top	98	0.1844	2.1	143.04	184.95	295.85	286.30	285.81	288.21	297.26	290.32	296.14	296.73	176.43	0.17	98.95
	0.13	Bottom	27	0.07862	2.1	128.99	186.09	294.72	289.57	290.05	289.45	295.39	289.02	294.17	295.84	178.91	6.61	56.52
	0.13	Bottom	27	0.07862	2.1	139.68	203.88	294.17	292.12	291.81	290.87	295.05	288.52	293.86	295.15	178.65	5.88	61.62
	0.13	Bottom	27	0.07862	2.1	127.79	187.45	294.44	293.19	292.82	291.95	296.81	291.09	293.90	297.00	177.00	5.35	65.28
	0.13	Middle	62	0.07862	2.1	139.78	194.87	294.43	289.67	291.34	289.90	294.82	291.23	294.21	295.27	178.64	4.52	70.92
	0.13	Middle	62	0.07862	2.1	129.88	181.46	294.65	291.43	290.58	288.33	295.79	289.94	294.46	296.72	177.98	4.20	73.07
	0.13	Middle	62	0.07862	2.1	128.52	187.79	294.73	290.20	291.54	289.47	295.54	290.73	294.46	296.06	178.38	3.36	78.64
	0.13	Top	98	0.07862	2.1	251.52	148.91	294.13	255.29	264.46	250.61	295.73	242.65	293.71	297.05	182.84	0.27	98.34
	0.13	Top	98	0.07862	2.1	127.78	216.17	294.40	282.80	289.34	289.61	295.65	288.36	294.16	297.39	177.88	1.03	93.63
	0.13	Top	98	0.07862	2.1	139.55	207.12	295.03	278.34	284.93	285.16	296.15	285.85	294.78	296.35	177.79	1.24	92.27
	0.13	Top	98	0.07682	2.1	122.62	187.89	294.94	289.49	289.16	289.55	295.39	287.23	294.68	295.84	178.45	1.19	92.61

7.5 Shot Tower Data Continued

	Shot Dia	Pos	Pos (in)	Gas Flowrate (LPM)	Res T1 (K)	Shot inlet T2 (K)	T3 (K)	T4 (K)	T5 (K)	T6 (K)	T7 (K)	T8 (K)	T9 (K)	T10 (K)	T11 (K)	T12 (K)	T13 (K)	Gas In (K)	%CO2	Capture
old	0.085	Bottom	33	2.1	132.59	207.26	242.08	242.09	240.51	243.21	247.24	247.73	243.64	244.95	245.20	673.34	233.11	179.35	2.80	82.31
	0.085	Bottom	33	2.1	140.73	194.56	233.64	233.69	232.02	234.36	240.63	242.51	249.07	252.79	253.10	732.89	238.88	184.42	2.81	82.23
	0.085	Bottom	33	2.1	129.59	202.44	229.55	229.11	227.86	232.40	239.52	242.78	244.46	248.77	249.67	809.49	234.27	177.95	2.76	82.59
	0.085	Bottom	33	2.1	154.33	204.12	230.08	229.21	227.21	227.53	233.15	235.77	239.06	244.40	245.01	675.13	233.35	178.78	2.91	81.58
	0.085	Bottom	33	2.1	149.95	210.82	255.85	256.51	255.20	258.57	261.92	261.04	256.14	256.06	255.74	630.84	234.35	179.45	2.90	81.64
	0.085	Middle	65	2.1	183.92	233.45	269.96	269.67	267.32	265.66	256.57	266.93							1.50	90.67
	0.085	Middle	65	2.1	110.74	197.88	259.04	260.54	259.16	260.08	263.98	263.15	262.56	264.34	264.16	867.81	237.63	178.46	1.36	91.52
	0.085	Middle	65	2.1	140.11	208.36	256.46	256.72	254.46	250.63	253.22	252.10	250.89	254.14	254.24	971.31	236.54	178.82	1.16	92.82
	0.085	Middle	65	2.1	148.94	230.78	255.07	254.69	252.56	251.20	254.50	254.49	256.12	259.12	259.15	987.03	235.36	177.99	1.47	90.85
	0.085	Middle	65	2.1	152.51	238.45	274.11	275.34	271.16	267.91	269.63	267.80	266.81	269.59	269.50	561.18	268.84	178.22	1.22	92.41
	0.085	Middle	81	2.1	137.58	231.40	268.06	268.06	265.36	263.58	265.73	266.97	267.61	270.86	270.91	790.04	240.47	177.97	0.51	96.85
	0.085	Middle	81	2.1	141.76	231.64	265.36	265.42	262.65	258.92	259.65	259.27	254.93	256.38	256.38	881.75	236.13	178.46	0.61	96.25
	0.085	Middle	81	2.1	127.22	182.53	223.51	223.14	221.73	223.11	227.00	228.77	227.42	229.15	229.71	753.45	229.20	177.57	0.59	96.35
	0.085	Middle	81	2.1	157.24	226.32	251.34	250.70	247.87	244.10	245.46	245.66	246.20	250.35	250.82	957.39	234.40	178.76	0.41	97.45
	0.085	Middle	81	2.1	137.71	188.41	209.34	209.28	208.76	215.33	225.19	232.32	233.33	234.85	235.09	712.91	228.61	177.95	0.50	96.91
	0.085	Middle	96	2.1	136.10	156.72	246.31	248.43	247.75	252.02	258.03	257.49	254.66	257.24	257.09	788.90	235.82	178.13	0.22	98.63
	0.085	Middle	96	2.1	134.07	215.60	269.04	271.00	265.30	264.42	266.23	264.68	262.85	266.22	266.23	939.77	267.31	179.98	0.16	99.01
	0.085	Middle	96	2.1	130.83	232.66	274.19	276.06	273.07	271.02	273.35	272.20	268.78	268.56	268.21	613.80	267.08	179.54	0.36	97.76
	0.085	Middle	96	2.1	148.78	232.03	267.64	268.59	264.78	259.77	262.97	262.20	260.57	263.74	263.87	601.05	265.47	175.89	0.23	98.58
	0.085	Middle	118	2.1	162.08	221.09	236.56	236.19	233.23	231.75	236.21	238.97	243.62	249.39	250.12	779.95	234.26	177.18	0.14	99.17
	0.085	Middle	118	2.1	153.29	216.15	263.09	264.97	260.49	255.51	258.15	257.33	256.02	261.08	261.53	543.76	266.98	177.48	0.06	99.61
	0.085	Middle	118	2.1	136.92	220.37	268.64	269.39	851.65	259.91	262.37	261.36	259.62	264.57	265.07	431.88	270.53	174.75	0.11	99.32
	0.085	Top	129	2.1	141.95	235.28	266.53	269.59	266.36	265.15	267.56	267.32	267.34	270.53	270.47	575.43	270.21	176.49	0.08	99.50
	0.085	Top	129	2.1	148.64	227.32	267.89	270.49	266.43	262.91	264.89	264.04	262.23	265.26	265.39	695.50	266.47	177.96	0.03	99.82
	0.085	Top	129	2.1	153.29	216.15	263.09	264.97	260.49	255.51	258.15	257.33	256.02	261.08	261.53	543.76	266.98	177.48	0.06	99.61
	0.08	Top	118	2.1	118.97	207.28	262.48	263.19	258.00	249.93	254.30	253.28	251.28	256.52	257.11		262.13	176.34	0.14	99.09

7.6 DTGT Particle Model

The droplets/particles in this model exhibit one-dimensional, transient variations in temperature, composition, and velocity that are described by energy, mass/mol species, and momentum equations, respectively.

7.7 Transport Equation

The following discussion develops quantitative techniques to describe transient, one-dimensional mass, momentum, energy, and species transport in a particle of arbitrary size and shape. The one dimension described is in the direction normal to a surface, that is, the radial direction in cylindrical and spherical particles and the shortest spatial dimension in the case of a rectilinear particle. In this document, this dimension is referred to as the radial direction even though such terminology is not strictly appropriate for a rectilinear particle. The specific assumptions are

1. All velocities in directions other than radial are zero
2. Gradients in all variables in directions other than radial are zero
3. The general particle shape does not change in time, though the size does.
4. There are no pressure-driven size changes in the particle.

If T represents temperature, the energy transport equation describes bulk energy transport under these assumptions as follows:

$$\rho\, c_p \left(\frac{\partial T}{\partial t} + v_r \frac{\partial T}{\partial r}\right) = \frac{1}{r^n}\frac{\partial}{\partial r}\left(k\, r^n\, \frac{\partial T}{\partial r}\right) + q$$

where all variables have their normal definitions, all parameters such as density, heat capacity, radial velocity, thermal conductivity, and volumetric heat source terms depend on r and on t, and where n is real-valued coefficient that indicates particle shape as follows:

Shape parameters for the general transport equation

shape	n
flat plate	0
cylinder	1
sphere	2

A more general transport expression useful for mass, momentum, and energy transport is

$$A\left(\frac{\partial f}{\partial t} + v_r \frac{\partial f}{\partial r}\right) = \frac{1}{r^n}\frac{\partial}{\partial r}\left(B\, r^n\, \frac{\partial f}{\partial r}\right) + S$$

where f represents a scalar dependent variable (temperature, mole/mass fraction, velocity component), S is a volumetric source term, the placeholder variables A, B and S represent generic transient, Fickian exchange coefficient, and volumetric source factors, respectively. The following table indicates specific values for these parameters depending on the quantity described by the transport equation, where all the variables have their normal meanings and appear in the nomenclature table.

Shape parameters for the general transport equation

Transported quantity	f	A	B	S
heat	T	ρc_p	k	q
species moles*	y_i	c	$c\,\mathcal{D}_{im}$	r_i
species mass	x_i	ρ	$\rho\,\mathcal{D}_{im}$	$\hat{r}_i$
momentum	v_r	ρ	μ	$-\frac{\partial p}{\partial r} + \rho g_r + S_\mu$

*velocity in this expression should be a mole-averaged rather than the almost universally used mass-averaged velocity. These quantities are the same for flows in which the preferential, usually diffusive, velocity of individual species is small compared to the average velocity. Boundary conditions for this expression are discussed later.

7.8 Second-order Spatial Solution

Assume that the dependent function, f, depends quadratcially on a spatial variable, r, that is,

$$f = a + b\,r + c\,r^2$$

If the value of the function is known at any three unique spatial points, designated as (r_1, f_1), (r_2, f_2) and (r_3, f_3), which need not be sequential, evenly spaced, or even contiguous on a grid, the coefficients a, b and c depend on these values as follows:

$$a = \frac{f_3 r_1 (r_1 - r_2) r_2 + r_3 (f_1 r_2 (r_2 - r_3) + f_2 r_1 (r_3 - r_1))}{(r_1 - r_2)(r_1 - r_3)(r_2 - r_3)}$$

$$b = \frac{f_3(r_2^2 - r_1^2) + f_2(r_1^2 - r_3^2) + f_1(r_3^2 - r_2^2)}{(r_1 - r_2)(r_1 - r_3)(r_2 - r_3)}$$

$$c = \frac{\frac{f_1 - f_3}{r_1 - r_3} + \frac{-f_2 + f_3}{r_2 - r_3}}{r_1 - r_2}$$

The derivatives of the function are

$$\frac{\partial f}{\partial r} = b + 2cr$$

and

$$\frac{\partial^2 f}{\partial r^2} = 2c$$

Using these expressions in the energy transport equation yields

$$\begin{aligned} k\{&f_1(r_2 - r_3)[n(r_2 + r_3) - 2(1+n)r] + f_2(r_3 - r_1)[n(r_1 + r_3) - 2(1+n)r] \\ &+ f_3(r_1 - r_2)[n(r_1 + r_2) - 2(1+n)r]\} \\ &+ r\left\{\left(k' - \rho c_p v_r\right)[f_1(r_2 - r_3)(r_2 + r_3 - 2r) + f_2(r_3 - r_1)(r_1 + r_3 - 2r) \right. \\ &\left. + f_3(r_1 - r_2)(r_1 + r_2 - 2r)] + (r_1 - r_2)(r_3 - r_1)(r_2 - r_3)\left(q - \rho c_p \frac{\partial f}{\partial t}\right)\right\} = 0 \end{aligned}$$

This expression is a function of r in addition to being a function of r_1, r_2 and r_3. That is, this function applies to any position r based on the three arbitrary locations r_1, r_2 and r_3. Since the relationship among the points r_1, r_2 and r_3 is to point in the discussion completely arbitrary, that is, they are not necessarily assumed to be in sequential order or even next to one another, the function should have identical dependencies on each point. That is, the subscripts for the points and the corresponding values of the function, if changed arbitrarily, will not change the function. Inspection of the equation verifies that this is true. The parameters k, $k' = \frac{\partial k}{\partial r}$, $\frac{\partial f}{\partial t}$, ρ, c_p and q, all of which can and generally do depend on r, are evaluated at r (not r_1, r_2 or r_3).

Evaluating the previous function at $r = r_2$ yields

$$\begin{aligned} k\{&f_1(r_2 - r_3)[n(r_2 + r_3) - 2(1+n)r_2] + f_2(r_3 - r_1)[n(r_1 + r_3) - 2(1+n)r_2] \\ &+ f_3(r_1 - r_2)[n(r_1 + r_2) - 2(1+n)r_2]\} \\ &+ r_2\left\{\left(k' - \rho c_p v_r\right)[f_1(r_2 - r_3)(r_3 - r_2) + f_2(r_3 - r_1)(r_1 + r_3 - 2r_2) \right. \\ &\left. + f_3(r_1 - r_2)(r_1 - r_2)] + (r_1 - r_2)(r_3 - r_1)(r_2 - r_3)\left(q - \rho c_p \frac{\partial f_2}{\partial t}\right)\right\} = 0 \end{aligned}$$

or, more simply and compactly,

$$\begin{aligned} k\{&f_1(r_2 - r_3)[(2+n)r_2 - nr_3] + f_2(r_1 - r_3)[n(r_1 + r_3) - 2r_2(n+1)] \\ &- f_3(r_1 - r_2)[nr_1 - (2+n)r_2]\} \\ &+ r_2\left\{\left(k' - \rho c_p v_r\right)[f_1(r_2 - r_3)^2 + f_2(r_1 - r_3)(r_1 - 2r_2 + r_3) - f_3(r_1 - r_2)^2] \right. \\ &\left. + (r_1 - r_2)(r_1 - r_3)(r_2 - r_3)\left(q - \rho c_p \frac{\partial f_2}{\partial t}\right)\right\} = 0 \end{aligned}$$

Collecting similar f_i factors yields

$$f_1\{k(r_2-r_3)[(2+n)r_2-nr_3]+r_2(k'-\rho c_p v_r)(r_2-r_3)^2\}$$
$$+f_2\{k(r_1-r_3)[n(r_1+r_3)-2r_2(n+1)]$$
$$+r_2(k'-\rho c_p v_r)(r_1-r_3)(r_1-2r_2+r_3)\}$$
$$-f_3\{k(r_1-r_2)[nr_1-(2+n)r_2]+r_2(k'-\rho c_p v_r)(r_1-r_2)^2\}$$
$$=-r_2(r_1-r_2)(r_1-r_3)(r_2-r_3)\left(q-\rho c_p\frac{\partial f_2}{\partial t}\right)$$

7.9 Boundary Conditions

The above equation requires two boundary conditions for a complete solution. The following discussion addresses two types of boundary conditions: a symmetry condition generally applied at the particle center and a surface condition that generally involves both the derivative of the function and the function value at the surface.

7.9.1 Symmetry Boundary Condition

The boundary condition at the center of a spherical particle is that the properties are symmetric, which generally means the derivative is zero.

$$\frac{\partial f}{\partial r}=0=b+2cr=\frac{f_3(r_2^2-r_1^2)+f_2(r_1^2-r_3^2)+f_1(r_3^2-r_2^2)}{(r_1-r_2)(r_1-r_3)(r_2-r_3)}+2r\frac{\frac{f_1-f_3}{r_1-r_3}+\frac{-f_2+f_3}{r_2-r_3}}{r_1-r_2}$$
$$=f_1(2r-r_2-r_3)(r_2-r_3)+f_2(r_1+r_3-2r)(r_1-r_3)+f_3(2r-r_1-r_2)(r_1-r_2)$$

This, also, is a function of r. If we presume that the particle center is at $r = r_1$, this becomes

$$f_1(2r_1 - r_2 - r_3)(r_2 - r_3) - f_2(r_1 - r_3)^2 + f_3(r_1 - r_2)^2 = 0$$

Commonly, the value of r at the center of the particle is 0, yielding a simpler expression, namely,

$$f_1(r_3 + r_2)(r_3 - r_2) - f_2(r_1 - r_3)^2 + f_3(r_1 - r_2)^2 = f_1(r_2^2 + r_3^2) + f_2 r_3^2 - f_3 r_2^2 = 0$$

7.9.2 Surface Boundary Condition

The boundary condition at the particle external surface is that the fluxes at the surface and the surface heat generation must balance

$$q = -k\frac{\partial T}{\partial r}\Big|_{r=R} = h\theta(T_s - T_\infty) + \epsilon\sigma(T_s^4 - T_r^4) + q_s$$

$$\begin{aligned} k\{&f_1(r_2 - r_3)[n(r_2 + r_3) - 2(1+n)r] + f_2(r_3 - r_1)[n(r_1 + r_3) - 2(1+n)r] \\ &+ f_3(r_1 - r_2)[n(r_1 + r_2) - 2(1+n)r]\} \\ &+ r\left\{\left(k' - \rho c_p v_r\right)[f_1(r_2 - r_3)(r_2 + r_3 - 2r) + f_2(r_3 - r_1)(r_1 + r_3 - 2r) \right. \\ &\left. + f_3(r_1 - r_2)(r_1 + r_2 - 2r)] + (r_1 - r_2)(r_3 - r_1)(r_2 - r_3)\left(q - \rho c_p \frac{\partial f}{\partial t}\right)\right\} = 0 \end{aligned}$$

$$h\theta T_\infty (r_1 - r_2)(r_1 - r_3)(r_2 - r_3)$$
$$+ k[f_3(r_1 - r_2)(2r + r_1 + r_2) - f_2(r_1 - r_3)(2r + r_1 + r_3)$$
$$+ f_1(r_2 - r_3)(2r + r_2 + r_3)]$$
$$= (r_1 - r_2)(r_1 - r_3)(r_2 - r_3)[q_s + \epsilon\sigma(T_s^4 - T_r^4) + h\theta f_3]$$

If we presume that the surface is at r_3, and set $T_s = T_3 = f_3$, this simplifies to

$$-k[f_3(r_1 - r_2)(r_1 + r_2 - 2r_3) - f_2(r_1 - r_3)^2 + f_1(r_2 - r_3)^2]$$
$$+ (r_1 - r_2)(r_1 - r_3)(r_2 - r_3)[h\theta(f_3 - f_{\text{blk}}) + q_s + \epsilon\sigma(f_3^4 - T_r^4)] = 0$$

or, collecting factors for f_i,

$$f_1 k(r_2 - r_3)^2 - f_2 k(r_1 - r_3)^2$$
$$+ f_3(r_1 - r_2)[k(r_1 + r_2 - 2r_3) - (r_1 - r_3)(r_2 - r_3)(h\theta + \epsilon\sigma f_3^3)]$$
$$= -(r_1 - r_2)(r_1 - r_3)(r_2 - r_3)(q_s + h\theta f_{\text{blk}} + \epsilon\sigma T_r^4)$$

7.10 Transient Solution

The transient term in the transport equation can be solved as analytically based solutions or finite-difference-based solutions, as described below.

7.10.1 Analytically Based Solution

The transport equation can be written as an explicit function of the temporal derivative as follows:

$$
\begin{aligned}
r_2(r_1-r_2)(r_1-r_3)(r_2-r_3)\rho c_p \frac{\partial f_2}{\partial t} \\
&= f_1\{k(r_2-r_3)[(2+n)r_2-nr_3]+r_2(k'-\rho c_p v_r)(r_2-r_3)^2\} \\
&+ f_2\{k(r_1-r_3)[n(r_1+r_3)-2r_2(n+1)] \\
&+ r_2(k'-\rho c_p v_r)(r_1-r_3)(r_1-2r_2+r_3)\} \\
&- f_3\{k(r_1-r_2)[nr_1-(2+n)r_2]+r_2(k'-\rho c_p v_r)(r_1-r_2)^2\} \\
&- qr_2(r_1-r_2)(r_1-r_3)(r_2-r_3)
\end{aligned}
$$

With respect to f_2, this is an ordinary, linear (assuming time-independent values of the parameters), first-order differential equation with the solution

$$
f_2 = \frac{B+Cq-\mathrm{e}^{-\frac{A\Delta t}{c_p\rho C}}(B-Af_2^0+Cq)}{A} = f_2^0\mathrm{e}^{-\frac{A\Delta t}{c_p\rho C}} + \frac{(B+Cq)\left(1-\mathrm{e}^{\frac{A\Delta t}{c_p\rho C}}\right)}{A}
$$

where Δt is the time since $f_2 = f_2^0$, A depends on spatial locations and transport parameters but not on any values of f_i, B depends on spatial locations and transport parameters and on f_1 and f_3 but not f_2, and C depends only on spatial locations. The asymptotic limit of this equation with respect to infinite time is

$$\lim_{\Delta t \to \infty} f_2 = \frac{B + Cq}{A}$$

The limiting value for short time increments is the initial value, as expected, i.e.,

$$\lim_{\Delta t \to 0} f_2 = f_2^0$$

The division by A can be eliminated by writing

$$Af_2 = (B + Af_2^0 + Cq)\mathrm{e}^{-\frac{At}{c_p \rho C}} - (B + Cq) = (B + Cq)\left(\mathrm{e}^{-\frac{At}{c_p \rho C}} - 1\right) + Af_2^0 \mathrm{e}^{-\frac{At}{c_p \rho C}}$$

or

$$Af_2 + (B + Cq)\left(1 - \mathrm{e}^{-\frac{At}{c_p \rho C}}\right) = Af_2^0 \mathrm{e}^{-\frac{At}{c_p \rho C}}$$

or, collecting terms that depend on f_i on one side of the equation,

$$Af_2 + B\left(1 - \mathrm{e}^{-\frac{At}{c_p \rho C}}\right) = -Cq + (Af_2^0 + Cq)\mathrm{e}^{-\frac{At}{c_p \rho C}}$$

where

$$A = (r_1 - r_3)\{k[n(r_1 + r_3) - 2(1 + n)r_2] + r_2(r_1 - 2r_2 + r_3)(k' - \rho c_p v_r)\}$$

$$B = f_1(r_2 - r_3)\{k[(2+n)r_2 - nr_3] + r_2(r_2 - r_3)(k' - \rho c_p v_r)\}$$
$$- f_3(r_1 - r_2)\{k[nr_1 - (2+n)r_2] + (r_1 - r_2)r_2(k' - \rho c_p v_r)\}$$
$$= -k\{f_3(r_1 - r_2)[nr_1 - (2+n)r_2] + f_1(r_2 - r_3)[(2+n)r_2 - nr_3]\}$$
$$+ r_2[f_1(r_2 - r_3)^2 - f_3(r_1 - r_2)^2](k' - \rho c_p v_r)$$

and

$$C = (r_1 - r_2)r_2(r_1 - r_3)(r_2 - r_3)$$

This leads to the following expression indicating all dependencies on f_i

$$Af_2 - \big(f_1(r_2 - r_3)\{k[(2+n)r_2 - nr_3] + r_2(r_2 - r_3)(k' - \rho c_p v_r)\}$$
$$- f_3(r_1 - r_2)\{k[nr_1 - (2+n)r_2] + (r_1 - r_2)r_2(k' - \rho c_p v_r)\}\big)\left(1 - \mathrm{e}^{-\frac{A\Delta t}{c_p \rho C}}\right)$$
$$= Cq + (Af_2^0 + Cq)\mathrm{e}^{-\frac{A\Delta t}{c_p \rho C}}$$

7.10.2 Finite-difference Solution

An alternative to the above approach is to approximate $\frac{\partial T}{\partial t}$ with $\frac{(T_2 - T_2^0)}{\Delta t}$, which yields

$$k\{f_3(r_1-r_2)[nr_1-(2+n)r_2]+f_1(r_2-r_3)[nr_3-(2+n)r_2]$$
$$-f_2(r_1-r_3)[n(r_1+r_3)-2(1+n)r_2]\}$$
$$+(r_1-r_2)r_2(r_1-r_3)(r_2-r_3)\left(\frac{\rho c_p(f_2-f_2^0)}{\Delta t}-q\right)$$
$$+r_2[f_3(r_1-r_2)^2-f_1(r_2-r_3)^2-f_2(r_1-r_3)(r_1-2r_2+r_3)]\left(k'-\rho c_p v_r\right)=0$$

Collecting like f_i terms yields

$$f_1\left\{k(r_2-r_3)[n(r_2+r_3)-2(1+n)r_2]-r_2(r_2-r_3)^2\left(k'-\rho c_p v_r\right)\right\}$$
$$+f_2\left\{\frac{\rho c_p(r_1-r_2)r_2(r_1-r_3)(r_2-r_3)}{\Delta t}-k(r_1-r_3)[n(r_1+r_3)-2(1+n)r_2]\right.$$
$$\left.-r_2(r_1-r_3)(-r_1+2r_2-r_3)\left(k'-\rho c_p v_r\right)\right\}$$
$$+f_3\left\{k(r_1-r_2)[n(r_1+r_2)-2(1+n)r_2]+r_2(r_1-r_2)^2\left(k'-\rho c_p v_r\right)\right\}$$
$$=(r_1-r_2)r_2(r_1-r_3)(r_2-r_3)\left(q+\frac{\rho c_p f_2^0}{\Delta t}\right)$$

Solving for f_2 yields

$$f_2=\frac{B+C\left(q+\frac{\rho c_p f_2^0}{\Delta t}\right)}{A+C\frac{\rho c_p}{\Delta t}}$$

where A, B, and C have the same definitions as in the analytical derivation. In the limit of $\Delta t\to\infty$, this expression also becomes

$$\lim_{\Delta t \to \infty} f_2 = \frac{B + Cq}{A}$$

As in the previous case, the limiting value for small time increments is the initial value, i.e.,

$$\lim_{\Delta t \to 0} f_2 = f_2^0$$

While both expressions have the same limits at both short and long times, the function values differ significantly between these limits, with the analytical solution responding more quickly in time than the finite-difference approximation.

7.11 Tower Model

7.11.1 Transport Equations

The heat transfer tower has both axial and radial gradients in temperature, composition, and velocity. Steady-state mass, momentum, and energy balances in two dimensions are solved to describe this tower as follows

$$\rho\left(v_r\frac{\partial v_r}{\partial r} + v_z\frac{\partial v_r}{\partial z} - \frac{v_\theta^2}{r}\right) = -\frac{\partial p}{\partial r} + \rho g_r + \frac{1}{r^n}\frac{\partial}{\partial r}\left(r^n\mu\frac{\partial v_r}{\partial r}\right) + \frac{\partial}{\partial z}\left(\mu\frac{\partial v_r}{\partial z}\right) + S_{\mu,r}$$

$$\rho\left(v_r\frac{\partial v_z}{\partial r} + v_z\frac{\partial v_z}{\partial z}\right) = -\frac{\partial p}{\partial z} + \rho g_z + \frac{1}{r^n}\frac{\partial}{\partial r}\left(r^n\mu\frac{\partial v_z}{\partial r}\right) + \frac{\partial}{\partial z}\left(\mu\frac{\partial v_z}{\partial z}\right) + S_{\mu,z}$$

$$\rho\, c_p\left(v_r\frac{\partial T}{\partial r} + v_z\frac{\partial T}{\partial z}\right) = \frac{1}{r^n}\frac{\partial}{\partial r}\left(r^n k\frac{\partial T}{\partial r}\right) + \frac{\partial}{\partial z}\left(k\frac{\partial T}{\partial z}\right) + S_q$$

$$\rho\left(v_r\frac{\partial x_i}{\partial r} + v_z\frac{\partial x_i}{\partial z}\right) = \frac{1}{r^n}\frac{\partial}{\partial r}\left(r^n\rho\mathcal{D}_{i,m}\frac{\partial x_i}{\partial r}\right) + \frac{\partial}{\partial z}\left(\rho\mathcal{D}_{i,m}\frac{\partial x_i}{\partial z}\right) + r_i + S_i$$

$$c\left(v_r\frac{\partial y_i}{\partial r}+v_z\frac{\partial y_i}{\partial z}\right)=\frac{1}{r^n}\frac{\partial}{\partial r}\left(r^n\rho\mathcal{D}_{i,m}\frac{\partial y_i}{\partial r}\right)+\frac{\partial}{\partial z}\left(\rho\mathcal{D}_{i,m}\frac{\partial y_i}{\partial z}\right)+r_i+\hat{S}_i$$

$$\frac{1}{r^n}\frac{\partial}{\partial r}(r^n\rho v_r)+\frac{\partial}{\partial z}(\rho v_z)=S_m=\sum_i S_i$$

All but the continuity equation are of the form

$$A\left(v_r\frac{\partial f}{\partial r}+v_z\frac{\partial f}{\partial z}+B\right)=\frac{1}{r^n}\frac{\partial}{\partial r}\left(C\,r^n\,\frac{\partial f}{\partial r}\right)+\frac{\partial}{\partial z}\left(C\frac{\partial v_r}{\partial z}\right)+\mathcal{R}+S$$

where f represents a scalar dependent variable (temperature, mole/mass fraction, velocity component), S is a volumetric source term, the placeholder variables A, B, C and S represent generic transient, swirl flow, Fickian exchange coefficient, and volumetric source factors, respectively. The following table indicates specific values for these parameters depending on the quantity described by the transport equation, where all the variables have their normal meanings and appear in the nomenclature table.

Parametric assignments for the two-dimensional, steady-state, rectilinear and cylindrical Tower transport equations

Transported quantity	$\boldsymbol{f}$	$\boldsymbol{A}$	$\boldsymbol{B}$	$\boldsymbol{C}$	$\boldsymbol{S}$
heat/temperature	T	ρc_p	0	k	$q+\mu\Phi_v+S_q$
species moles*	y_i	c	0	$c\,\mathcal{D}_{im}$	S_m
species mass	x_i	ρ	0	$\rho\,\mathcal{D}_{im}$	$\hat{S}_m$
radial momentum/velocity	v_r	ρ	0	μ	$-\frac{\partial p}{\partial z}+\rho g_z+S_{\mu,r}$
axial momentum/velocity	v_z	ρ	$-\frac{v_\theta^2}{r}$	μ	$-\frac{\partial p}{\partial z}+\rho g_z+S_{\mu,z}$

Following the same procedure as in the previous section, these equations are solved using second-order approximations. There are subtleties in these equations that are not obvious, even

to those accustomed to using them. Specifically, the reaction component of the source term and the mass source term, although looking to be very similar, differ fundamentally. The reaction component is for materials that change compositions within a given phase, with no change in mass of the phase. In the applications here, materials transform from one phase to another. The mass/mole source term handles this type of transformation. The importance of the distinction can be appreciated by considering a simplified case of 1-D, steady transport in which convection dominates diffusion (diffusion is negligible). The transport equation for an inert ($r_i = 0$) component of the gas phase in this case would be

$$\rho v_z \frac{\partial x_i}{\partial z} = S_m$$

If S_m were not included, in addition to S_i, in the equation, the implication is that the gradient in the inert component mass fraction is zero. This is clearly not the case. If, for example, CO_2 is condensing in the flow, then the mole fractions of both CO_2 and N_2 should both be changing. However, N_2 does not react, so r_i is zero. The prediction without the source term will not predict this corN_2 correctly. It will also not predict CO_2 correctly without the source term in addition to the reaction term, but the error in the prediction is not as easily illustrated. The source term is not specific to the species being balanced, that is, it is not $S_{m,i}$, bur rather it is the total change in mass/moles in the system. For mass, and assuming

$$S_m = \sum_i r_i$$